

Numerical simulation of particle impact drilling (PID) systems: A one-way coupled approach

G. Casas^{a,b,*}, I. de-Pouplana^{a,b}, R. Gandikota^c, and E. Oñate^{a,b}

^a*CIMNE - Centre Internacional de Metodes Numerics en Enginyeria, Gran Capitán s/n, 08034 Barcelona, Spain*

^b*Departament d'Enginyeria Civil i Ambiental (DECA), Universitat Politècnica de Catalunya (UPC), Campus Nord, C. Jordi Girona, 1-3, 08034 Barcelona, Spain*

^c*MindMesh Inc. Houston, TX, USA*

October 2, 2020

Abstract

A numerical technique based on a CFD-DEM method is presented for the analysis of particle impact drilling (PID) systems. The method is build from a preexisting finite element Navier-Stokes solver for the fluid phase and a discrete element method module for the steel particles which this drilling technology utilizes to enhance the penetration rate. We provide a detailed description of the most relevant implementation issues, including our choice of the hydrodynamic forces appropriate for power-law fluids. We also discuss several critical aspects related to the validity of the simplifying assumptions that will be helpful to simulation engineers. We apply our simple, one-way coupled approach on designs provided by an industrial partner to illustrate its potential as an analysis tool for this promising drilling technology.

Keywords: particle impact drilling, discrete element method, CFD-DEM, finite element method, oil and gas.

1 Introduction

Particle-impact drilling (PID) refers to a special type of drilling technology for the oil and gas industry in which the principal rock-erosive mechanism is based on the impact of high-speed, particle-laden mud jets on the substrate, rather than on the abrasive action of the drill-bit cutters. PID systems are able to achieve greater rates of penetration than their traditional alternatives [37, 27] and are especially suited for boring through very hard rock [47, 59].

*Correspondence to: Guillermo Casas, CIMNE, Edificio C1, Campus Nord, UPC, Gran Capitán s/n, 08034 Barcelona, Spain. Email: gcasas@cimne.upc.edu

In essence, a PID drill-bit is similar to a conventional one: it consists of a cutter fixed at the end of a rotating tube through which the drilling mud is pumped from the surface. A set of openings allow the mud to flow out of the bit's tip, cleaning the cuttings and dragging them back to the surface through the annulus, i.e. the space contained between the outer surface of the tube and the hole's casing.

What sets PID systems apart are the small steel balls with which the drilling mud is laden. These balls are added to the drilling fluid on the surface and recycled through the system forming a relatively disperse, two-phase flow with the mud. The mix is transported to the bottom of the hole, where it is violently accelerated as it passes through any of the particularly narrow apertures (nozzles) positioned at the tip of the drill-bit, forming highly energetic jets. In these jets the fluid velocity can surpass 200m s^{-1} , transferring enough kinetic energy to the steel balls to effectively erode off material from the rocky bed upon impact. Indeed, most of the erosion is generated by this mechanism, although PID bits has a set of cutters nonetheless. Their role is complementary to that of the jets, providing extra penetration power in particularly hard rocks or an effective fall-back solution for cases in which the jets are insufficient or working sub-optimally. A schematic diagram of PID technology is shown in Figure 1.

Despite the observed higher rates of penetration and the conceptual simplicity of PID systems, their widespread use is still to materialize. In fact, there remain a number of challenges associated with the use of steel particle-laden jets that require further study, two of which are central to the present work:

First, it is important that the steel particles flow without trouble and do not accumulate, neither in the interior of the drill bit nor between the bit and the rock outside. Such accumulation could lead to several problems, including the clogging of the space through which the drilling mud must flow, or a drop in the penetration speed due to the shielding effect of the particles retained between the rocky bed and the drill bit.

Second, the presence of hard steel particles can generate an increased rate of wear on the drill bit. In particular, two different mechanisms can lead to this wear: 1) Fast moving particles that impact on the drill bit interior (in the acceleration phase) or its exterior (rebound), and 2) Accumulated particles that form a bed between the drill bit and the substrate. Both these issues provide criteria with respect to which it is possible to optimize the bit designs and specifications.

However, it is difficult and costly to set up experiments for every single design variation in order to provide the necessary data to evaluate its performance and guide future adjustments. And even if one could afford to run these experiments, the extraction of all the relevant data would still be a technical challenge. Therefore it is highly desirable to complement experimental investigations with numerical analysis. Indeed, numerical analysis has several advantages for the study of PID systems:

- It is relatively inexpensive.
- It has reduced limitations in terms of boundary conditions and material parameter values, even if the *ranges* of scales being represented simultaneously is, nevertheless, limited due to the associated numerical cost.
- It provides a great versatility in terms of the types of data to be produced and their attainable precision.

- Prototypes are much easier to modify as compared to physical models.

Despite these advantages, very little work has been reported about the use of numerical methods to the study the hydrodynamics of full PID systems. Among the few exceptions we find the works [19, 28, 49, 35, 68], all based on finite volume method, or the experimental work [67], that studied the rate of erosion of the substrate under different impact conditions.

In this work we present a numerical method based on a Lagrangian-Eulerian, point-particle approach [31, 56], where the flow disturbance caused by the particles is considered a fine detail and is not resolved by the computational mesh. The particles are treated as Lagrangian points and their motion is integrated based on the locally averaged fluid field. This requires knowledge about the background fluid field (the velocity and perhaps its derivatives) at the location of the particles. Since the fluid is not resolved around the point-particles, the computational mesh needs not be any finer than several times the particles radius, as long as the macroscopic behavior of the fluid is well-captured (Figure 3).

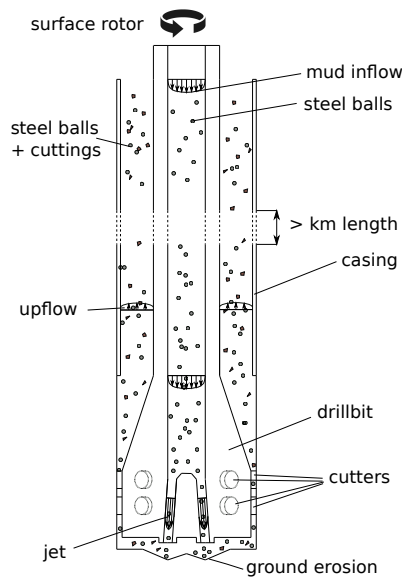


Fig. 1 Diagram of workings of the PID wellbore, showing inflow mud with steel particles, and up-flow cuttings wash-up.



Fig. 2 PID drill bit

In this paper we focus on the one-way only coupled approach. That is, we ignore the effect that the steel particles have on the flow. While somewhat rough, this assumption simplifies the problem enough that it is worth to explore the possibilities of this approach as a way to produce reasonable first approximations to the solution. This limits the number of unknown input parameters and simplifies the sensitivity analyses. Our first

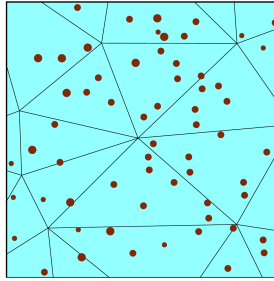


Fig. 3 Point-particle approach illustrated. The finite size of the particles is only relevant to compute their contact interactions, not to calculate their interaction with the fluid, for which only their center point (and radius) is of relevance.

goal is to describe a numerical strategy in detail, including all the necessary elements (fluid and particles models, drag force law, FEM discretization, time-stepping, post-process tips etc.) for the implementation of the numerical method. Our second goal is providing examples to illustrate the use of such a method for analysis of PID systems useful for the design of prototypes. Two-way coupled strategies will be the subject of future work.

The paper is organized as follows. Section 2 deals with the particle model chosen, introducing the basic equation of motion and summarizing the basics and discussing particularities relevant to the PID problem. Section 3 describes the basic equations that govern the motion of the fluid phase model and their finite element discretization. The previous two sections describe the fluid phase problems, basically as separate mathematical problems. In Section 4 the coupling strategy that links both solutions is described. Finally, in Section 5 we present example simulations to illustrate the potential of the proposed methodology for the analysis of PID systems.

2 Model for the steel particles

The steel particles are modelled as spheres and their motion is simulated using the discrete element method (DEM). Our particular implementation is largely standard and a complete description of the algorithm falls outside the scope of this work. Thus, the reader is referred to the standard literature on the subject (see [11] and references cited therein) for details about this numerical technique. In the following subsections we discuss a selection of topics specifically chosen for their relevance in relation to the problem at hand.

2.1 Basic ingredients of the DEM approach

Let us briefly review the fundamentals of the DEM algorithm. For a recent, widely general review on the subject, see [23]. The DEM consists in the numerical integration of the trajectories of a number of particles, that move according to Newton's laws

under the action of both external forces, such as their own weight, and contact forces that act between particles when they become close enough. The numerical integration is typically computed with a finite difference scheme, which in the great majority of implementations is explicit in nature. Here we will also follow this approach. The preference for explicit schemes has been justified in the literature [53] and the most extended opinion is that the cost of an implicit implementation would not be smaller or, at best, not justify its greater complexity and difficulty of implementation. Such view is not, nonetheless, universal [33].

In the simplest versions of the DEM, each particle is modelled as a rigid sphere, and its (rigid solid) movement is determined by the position of its center and its rotation vector, both of which are evolved in time by the integration scheme. The presence of bounding walls can in turn be modelled by a set of flat rigid faces. In our implementation the bounding surfaces are triangulated in the pre-process step, so that each resulting triangle defines a rigid face.

The most popular variety of the DEM, and the one used here, is called the *soft-sphere* method (as opposed to the hard-sphere method [50]). In this version the particles are allowed to overlap (slightly) over each other and also penetrate the walls. A given overlap is characterized by a point inside the overlap region, the contact point, and its magnitude is represented by a scalar δ_{indent} (the indentation or penetration) that measures how far into each neighbor the contact point has moved. Associated with it there is a contact force and, sometimes, also a contact moment, to be added to the total actions being applied to the particle. These contact forces and moments are typically functions of δ_{indent} and its derivatives, and sometimes of their histories too. The simplest versions include a linear spring and dash-pot rheological model, which depend linearly on δ_{indent} and $\dot{\delta}_{\text{indent}}$, although the contact model can become much more complicated, often devised with a particular application in mind. Typically, there exist a number of free parameters that allow to calibrate these micro-scale models by comparing the resulting macroscopic motion with experimental results. The particular contact model used in this work is described in Section 2.1.1.

Another crucial component of any DEM method is an efficient algorithm to determine the potential contacts that take place at every step of the calculation. In order to avoid the $O(N^2)$ (where N is the number of particles plus walls) scaling of brute-force check of all the possible overlaps, a suitable search algorithm is used to determine the correspondence between each particle and its neighbors. State-of-the-art algorithms achieve $O(N \log N)$ scaling or even $O(N)$ [64]. Specifically, we use a binning strategy for both particles and triangular elements for which the hierarchical method is applied [54]. The search is performed in an alternate fashion, between time-integration steps, often with a lower frequency than the time integration steps, as described in Section 2.2.

To summarize, the DEM algorithm looks like the one presented in Algorithms 1 and 2.

The equation of motion of the particles is given by

$$m_p \frac{d\mathbf{v}}{dt} = \xi_C \sum_{k_p=1}^{N_p} \mathbf{F}_{k_p} + \sum_{k_w=1}^{N_w} \mathbf{F}_{k_w} + \mathbf{F}_{\text{coup}} := \mathbf{F} \quad (1)$$

Algorithm 1 General DEM algorithm

```
1:  $t_{\text{DEM}} \leftarrow 0.0$  ▷ time
2:  $m \leftarrow 0$  ▷ steps
3: INITIALIZEPARTICLES() ▷ with the given initial conditions
4: SEARCHNEIGHBORS() ▷ Hierarchical method [54]
5: while  $t_{\text{DEM}} < t_{\text{End}}$  do
6:    $t_{\text{DEM}} \leftarrow t_{\text{DEM}} + \Delta t_{\text{DEM}}$ 
7:    $m \leftarrow m + 1$ 
8:   SOLVEDEM( $t_{\text{DEM}}, m$ ) ▷ Algorithm 2
```

Algorithm 2 Algorithm for function SOLVEDEM(t_{DEM}, m)

```
1: for  $p = 1, \dots, N_{\text{particles}}$  do ▷ for each particle
2:    $\mathbf{x}_{p,m+1} \leftarrow \text{UPDATEPOSITION}(\mathbf{x}_{p,m}, \mathbf{v}_{p,m})$  ▷ eq. (3a)
3:   MOVERIGIDPARTS( $t_{\text{DEM}}$ )
4:   if ISSEARCHSTEP( $N_{\text{search}}, m+1$ ) then ▷ search every  $N_{\text{search}}$  steps
5:     SEARCHNEIGHBORS() ▷ assign neighbors (particles + walls) to particles
6:     for  $p = 1, \dots, N_{\text{particles}}$  do ▷ force and moment on each  $p$  eq. (1)
7:        $\mathbf{F}_{p,m+1}^* \leftarrow \text{EXTERNALFORCES}(\mathbf{x}_{p,m+1}, \mathbf{v}_{p,m})$  ▷ weight and fluid interaction forces
8:       for  $q = 1, \dots, n_{\text{neigh},p}$  do ▷ for each neighboring particle
9:          $\mathbf{F}_{p,m+1}^* \leftarrow \mathbf{F}_{p,m+1}^* + \text{BALLTOBALLFORCE}(\mathbf{x}_{p,m+1}, \mathbf{v}_{p,m}, \mathbf{x}_{q,m+1}, \mathbf{v}_{q,m})$ 
10:      for  $r = 1, \dots, n_{\text{neigh},r}$  do ▷ for each neighboring wall
11:         $\mathbf{F}_{p,m+1}^* \leftarrow \mathbf{F}_{p,m+1}^* + \text{WALLTOBALLFORCE}(\mathbf{x}_{p,m+1}, \mathbf{v}_{p,m}, \mathbf{x}_{r,m+1}, \mathbf{v}_{r,m})$ 
12:      for  $p = 1, \dots, N_{\text{particles}}$  do ▷ for each particle
13:         $\mathbf{v}_{p,m+1} \leftarrow \text{UPDATEVELOCITY}(\mathbf{v}_{p,m}, \mathbf{F}_{p,m+1}^*)$  ▷ eq. (3b)
```

where m_p is the particle mass, k_p runs over all the neighboring particles, k_w over all neighboring triangular rigid walls, and where the binary parameter $\xi_C \in \{0, 1\}$ is introduced to easily turn off inter-particle interactions as required (such as in Section 5.7). The first two terms correspond to the contact forces, which are only *actually* computed if the corresponding neighboring wall or particle center fall within the ball centred at the target particle's center with radius equal to the *search radius*. The search radius is defined as the particle radius plus a tolerance that is tuned to optimize the computational cost. Such optimal cost is to be found as an ideal balance between the cost of running the search algorithm at every time step (necessary if the search tolerance is set to zero) and that of having a larger number of neighbors per particle as a result of the enlarged search tolerance; see Section 2.2. Finally, the additional term $\mathbf{F}_{\text{coupling}}$ has been added to represent the inter-phase force, which will be discussed in Section 4. Clearly all the variables in eq. (1), except for ξ_C , are different for different particles.

Furthermore, in many situations it is important to include the rotational degrees of freedom. The angular equation of motion reads

$$I_p \frac{d\omega}{dt} = \mathbf{T}_{\text{coup}} + \mathbf{T}_{\text{cont}} \quad (2)$$

where I_p is the moment of inertia of the particle (a scalar for a sphere, otherwise the whole inertia tensor should be used), where \mathbf{T}_{cont} is the sum of the moments due to the contact forces \mathbf{F}_{k_p} and \mathbf{F}_{k_w} in eq. (1) between overlapping particles and particles and solid surfaces. A term \mathbf{T}_{coup} is provided to model the moment applied by the fluid on the particle.

Remark. *One could additionally consider the contributions from contact moments directly applied at the contact point in eq. (2), which would need to be added to the moments produced by the contact forces; i.e., the rolling friction [63], although we ignore them here for conciseness*

Note that eqs. (1) and (2) neglect all fluid-mediated interactions between neighboring particles, what is sometimes called *three-way coupling* [40]. For possible extensions to include these effects see [4, 51]. The particular forms of the coupling force and moment are discussed in Section 4.1.

2.1.1 Contact model

The contact model is the rheological model that relates the kinematics of a contacting pair with the force and moment between both particles involved (a plane can be seen as an infinite-radius particle). The kinematics in the DEM contain a number of subtleties that we will not cover here, but they can be roughly characterized by the evolution of three degrees of freedom (DOFs) per contact pair: the instantaneous values of the indentation and its derivative (i.e. normal motion; one DOF) and the historically accumulated tangential motion and its derivatives (two DOFs). The latter is defined as the integral of the relative tangential motion projected onto the plane that passes through the contact point and is orthogonal to the segment joining the particles' centres. Note that for the tangential degrees of freedom it is necessary to store historical information,

since there is no way to derive the extension of the tangential springs from just the instantaneous relative positions of the particles involved [9].

Our contact model, which was proposed by [58] (see also [9]) includes a Hertzian spring-dashpot model with no sticking [48] for the normal motion and a Deresiewicz–Mindlin spring-dashpot model connected in series with a frictional element for the tangential motion. This normal element is characterized by the Young’s modulus of the material and the coefficient of normal restitution (COR), while the tangential one is characterized by a friction coefficient ($\mu_{p,q}$, where p and q identify the materials of the two particles involved) in addition to the Young’s modulus and a tangential viscous dissipation coefficient.

The COR is the ratio of the normal component of the post-rebound velocity over the same component of the incident velocity, and is generally bounded between zero and one. It is a useful engineering parameter that characterizes the amount of energy dissipated by an impact, depending on the nature of the materials involved. However, it must be kept in mind that the assumption of it being independent of the incident velocity is actually not entirely correct [34] and so the COR is not, strictly speaking, a *material parameter*, but only approximately so.

Both friction coefficient and the COR must be chosen to match the physical behavior of the material. However, the Young’s modulus can be altered without significantly modifying the macroscopic motion of the particles in certain circumstances. This possibility is very advantageous, since it allows to increase the time step substantially (Section 2.1.2).

2.1.2 Time integration scheme

In order to solve eq. (1) (together with a suitable initial condition $\mathbf{x}(0) = \mathbf{x}_0$), we use a finite difference scheme. Several options are possible but we have run our simulations using the a version of the two-step Adams–Bashforth scheme, which has been extensively tested. The difference equations are

$$\mathbf{x}_{n+1} = \mathbf{x}_n + \frac{\delta t}{2} (3\mathbf{v}_n - \mathbf{v}_{n-1}) \quad (3a)$$

$$\mathbf{v}_{n+1} = \mathbf{v}_n + \frac{\delta t}{2m_p + m_f} (3\mathbf{F}_n^* - \mathbf{F}_{n-1}^*) \quad (3b)$$

Where \mathbf{F}^* is the total force \mathbf{F} calculated at the current position minus the terms proportional to the acceleration of the particle in the added mass force (Section 4.1.1), which is treated implicitly by increasing the mass of the particle by $m_f/2$, where m_f is the mass of a volume of fluid displaced by the particle. This two-step scheme can be started with the analogue, first step version of the same algorithm. We have found this modification to improve stability when contact is taken into account. A similar algorithm is used for the integration of the angular motion.

Remark. *Note that, strictly speaking, we are not following eq. (3) in that the contact forces are being evaluated with a mix of updated position (\mathbf{x}_{n+1}) and old particle velocity (\mathbf{v}_n), as indicated in Algorithm 2.*

2.2 Scales

The introduction of soft-sphere DEM particles in the fluid dynamics simulation implies that a new, (short) time scale needs to be resolved: the contact time scale. In Section 2.1.1 we mentioned that our contact model (as in the most common DEM applications) is composed of an elastic element arranged in parallel with a dissipative element, typically of viscous nature. This kind of arrangement is known as a spring-dashpot model. The role of the dissipative element is to ensure that a correct amount of energy is lost at each impact, since no real (macroscopic) system is perfectly elastic.

Remark. *Note that intensity of the dissipation element cannot in general be tuned for numerical reasons, since it controls the value of the COR, which determines the amount of energy dissipated at each impact as mentioned above. This is a crucial physical property that affects the macroscopic behavior of the system, specially in collisional regimes [1] (the motion is mostly formed of a succession of collisions alternated with contact-less, ballistic motion).*

On the other hand, the action of the elastic element is typically less constrained by the physics, as long as it is stiff enough. Indeed, the fundamental reason for introducing the DEM method in the first place is that collisions are regarded as playing a non-negligible role in the simulation. Therefore, *at the very least*, it is always necessary to ensure the non-penetrability of the spheres through one another or through the walls. Nonetheless, it is often not necessary to reproduce the real stiffness of the material being simulated, as long as

1. Sufficient repulsion is achieved in all circumstances to avoid excessive penetration.
2. There is separation of scales [46], in time and space, between those dynamic scales associated with free flight and those associated with the process of rebound.
3. The resulting computed trajectories are not too far from possible ones at more realistic stiffnesses, as it might happen when extremely soft particles are able to unrealistically squeeze through a narrow hole.

In many DEM simulations, specifically those dealing with moderately dense to disperse regimes, such conditions can be achieved with stiffnesses significantly lower than the real ones. In such a case, the elastic contact model can be interpreted as a mere numerical device, reminiscent of the classic penalty model [62] in contact mechanics. Next the advantage of being able to consider an artificially low stiffness is explained.

Choosing the time step size. The selection of a suitable time step is crucially important in any DEM simulation, since it has a proportional impact on the numerical cost of the simulations. As in any finite difference calculation, one would like to select the time step based on the required accuracy, so as to minimize the total number of time steps. However, the choice is also restricted by the need to preserve numerical stability, which is always conditional to the size of the time step.

The analytical calculation of the optimal time step has been attempted in the past [45], mostly based on the use of approximations, such as the linearization of

the nonlinear force models to derive the critical time step of the mass-spring system for an arbitrary pair of contacting particles. However, such calculations are too complex in practice or lead to excessively rough estimates of little practical value. We have based our choice of the time step on experience, often requiring a certain number of iterations in order to attain a good compromise between accuracy and cost.

Nonetheless, we do not proceed blindly, but actually apply a criterion that we next describe and that will also provide an argument to explain the high computational demands of this numerical approach.

- The smallest scales represented in our simulations correspond to the contact dynamics, and consequently it is the contact that dictates the maximum allowable time step, not the interactions with the fluid (only the added mass force, F_A has a response time at a comparable time scale, but we are treating it implicitly).
- As discussed above, the stiffness of the contact model is considered a numerical parameter that can be softened to increase the critical time step for numerical stability. This practice is acceptable as long as the three criteria given above (sufficient repulsion, scales separation and realistic movement) are met.
- The contact must be properly resolved to avoid excessive numerical errors and spurious energy creation. This is guaranteed by dividing the contact duration in, at least 15 to 30 steps ([30]), depending on the numerical scheme.

According to this, we first calculate the minimal expected contact duration. In order to do that, we use the formula that can be found in [9] (see also [2]), valid for Hertzian contact. For Hertzian contact laws, the contact duration decreases with the impact velocity, so we use an estimate for the maximum impact velocity, which will be comparable to the fluid speed inside the nozzles, as a worst-case scenario. Once we have the minimal expected impact duration, we divide it by a large enough number, say fifteen, to bound the time step above. Finally, we apply a security factor to further reduce it. We have observed that using this technique leads to robust estimates for the optimal time step, limiting the need for trial-and-error. Typically, the resulting DEM time step is about 1000 times smaller than that used by the fluid solver (see Table 4).

2.3 Wear

It is interesting to be able to predict the level of wear on the different surfaces of the drill bit under the repeated impact of the steel particles. While a quantitative prediction is certainly challenging, there is certainly a great potential for the prediction of relevant qualitative trends, such as:

- the location of intense wear concentrations
- the sensitivity of the wear spread pattern upon changes in the design and operation parameters
- the identification of unexpected wear mechanisms
- the classification of frictional wear versus impact wear regions

We have implemented a simple wear model to illustrate these points. During the contact of a particle against a wall, a finite *impact wear* (ΔW_{impact}) contribution is calculated according to

$$\Delta W_{\text{impact}} \sim \rho_p d_p^2 U_n \quad (4)$$

where U_n is the normal relative velocity between the particle and the triangular surface and d_p is the particle diameter. This quantity is then divided by the face area and distributed to the nodes using the triangle's linear shape functions. Note that while the factors in eq. (4) surely contribute to the wear, we have arbitrarily set their effect to be multiplicative, as well as their powers for simplicity. The resulting units of W_{impact} are of mass per unit time and area; so it could be interpreted as the mass lost to erosion per unit area on the surface. A realistic model would require further investigations and this is left for future work.

2.4 Analytic tools

Taking advantage of the object-oriented philosophy of our solver (Kratos Multiphysics [20]), we have generalized the notion of the discrete element to that of the *analytic discrete element*. This type of element is designed to collect information during a simulation by increasing its associated data-structures in a trade-off of information vs. computational efficiency.

The basic concept consists in allowing a number of the discrete elements to be marked as analytic, behaving as the discrete element they generalize but performing a few extra operations and recording extra data. These elements are constantly monitored by an external process that collects the information stored in each of them. The specific data stored in the data structures associated with these discrete elements are best understood by example. Here we give a brief account of two variants of analytic element that we have implemented in our code.

2.4.1 Analytic particles

The analytic particle is a discrete element that interacts with other particles exactly like the rest but that keeps a record of the *impact data* associated to its contacting neighbors at a given time step. This means that the information is only related to a specific time step and thus must be collected at every time step or else it is lost. This design requires an operation to be added to the DEM solution with the same frequency as the DEM solution itself, but is only (relatively speaking) costly if the proportion of analytic particles is comparable to the total number of particles in the domain. The information collected from all the particles is stored in a database for later analysis. We use HDF5-format files to store and manage this data.

The reason of this design is to keep the data structures associated to the discrete elements as small as possible, so as to make the most out of the available cache. Having memory-wise very heavy particles would result in extremely slow computations overall, spoiling the efficiency of the program. By limiting the total number of possible simultaneous impacts to a few (in our case, only four), the data structures are kept at a fixed size, avoiding allocation/deallocation on the fly. Note that it is extremely unlikely that more than four impacts occur at exactly the same time step.

The precise information kept per impact may vary, but a useful combination is to keep the impact velocity (normal and tangential to the particle surface), the ID of the other particle and the positions at the moment of impact. This information can be used in simulations to keep track of the impact frequency and violence [26] and other aspects of the interaction, such as chemical exchanges, etc.

2.4.2 Analytic surfaces

By counting the triangular rigid faces as DEM elements too, one can generalize them in a similar way as we have explained with analytic particles. We have thus devised a type of analytic surface with the particularity of *not affecting the motion of contacting particles*. Instead, these surfaces make measurements of the particles as the latter traverse them. This allows, for example, to measure fluxes of particles. The versatility of the DEM rigid faces is inherited by these flux-measuring particles, which may be obtained from triangulations generated by applying the standard FEM mesher to any complicated cross-section. The information is again stored in appropriate HDF5 files for posterior analysis.

3 The continuous-phase problem

3.1 Fluid model

Let us describe the problem corresponding to the continuous phase when considered uncoupled to the disperse phase. We restrict our attention to incompressible fluids, the motion of which can be modelled by the Navier–Stokes equations:

$$\left. \begin{aligned} \rho_f \frac{\partial \mathbf{u}}{\partial t} + \rho_f (\mathbf{u} \cdot \nabla) \mathbf{u} - \mu \nabla^2 \mathbf{u} + \nabla p = \mathbf{f} \\ \nabla \cdot \mathbf{u} = 0 \end{aligned} \right\} \text{in } \Omega \times [0, T) \quad (5a)$$

$$(5b)$$

where \mathbf{u} is the fluid velocity, p is the pressure, \mathbf{f} is an external body force (for example, the specific weight), ρ_f is the density of the fluid and μ its viscosity.

Let us assume that the domain's boundary $\partial\Omega$ is partitioned into Dirichlet (Γ_D) and Neumann (Γ_N) parts with $\partial\Omega = \Gamma_D \cup \Gamma_N$ and $\Gamma_D \cap \Gamma_N = \emptyset$ and that the problem described by eq. (5) is completed with suitable initial and boundary conditions:

$$\mathbf{u} = \mathbf{u}_0 \quad \text{in } \Omega \times \{0\} \quad (6a)$$

$$\mathbf{u} = \mathbf{u}_D \quad \text{on } \Gamma_D \times [0, T) \quad (6b)$$

$$\boldsymbol{\sigma} \cdot \mathbf{n} = \mathbf{t}_N \quad \text{on } \Gamma_N \times [0, T) \quad (6c)$$

where \mathbf{u}_0 is the initial velocity field, \mathbf{u}_D the velocity fixed on Γ_D , \mathbf{n} the exterior unitary normal vector on Γ_N , \mathbf{t}_N the imposed surface traction on Γ_N , and where the Cauchy stress tensor $\boldsymbol{\sigma}$ is defined as

$$\boldsymbol{\sigma} = -p\mathbf{I} + \boldsymbol{\tau} \quad (7)$$

where $\boldsymbol{\tau}$ is the shear stress tensor.

The typical drilling mud used in the oil and gas industries has a non-Newtonian behaviour [17]. This means that its motion is not well-approximated by the standard Navier-Stokes equations, which assume the viscosity coefficient to be a constant. In this context, it is common to assume that the fluid is of a Herschel–Bulkley type [36] instead.

The constitutive equation for this type of fluids can be written as a generalized Newtonian fluid, where the constant viscosity is replaced by an *effective viscosity* μ_{eff} as a function of the flow. The shear stress $\boldsymbol{\tau}$ can be thereby defined as:

$$\boldsymbol{\tau} = 2\mu_{\text{eff}}(\dot{\boldsymbol{\gamma}})\boldsymbol{S} \quad (8)$$

where $\dot{\boldsymbol{\gamma}}$ is the local strain rate, given by

$$\dot{\boldsymbol{\gamma}} = \sqrt{2\boldsymbol{S} : \boldsymbol{S}} \quad (9)$$

with \boldsymbol{S} being the symmetric gradient of velocity.

In particular, a Herschel–Bulkley fluid the functional dependence of the effective viscosity on the strain rate reads

$$\mu_{\text{eff}} = \begin{cases} \mu_0 & \text{if } \dot{\boldsymbol{\gamma}} \leq \dot{\boldsymbol{\gamma}}_0 \\ K|\dot{\boldsymbol{\gamma}}|^{n-1} + \tau_0\dot{\boldsymbol{\gamma}}^{-1} & \text{if } \dot{\boldsymbol{\gamma}} > \dot{\boldsymbol{\gamma}}_0 \end{cases} \quad (10)$$

where μ_0 is such that there is continuity at $\dot{\boldsymbol{\gamma}} = \dot{\boldsymbol{\gamma}}_0$. The material parameters K and n are known as the flow *consistency index* and the *behaviour index* respectively. One distinguishes between *shear thinning* fluids ($n < 1$) and *shear thickening* fluids ($n > 1$). The fluid becomes less viscous with increasing shear rate in the former, while the opposite is true for the latter. Drilling muds are all of the shear thinning type [36].

3.2 Finite element discretization

The FEM is based on the weak version of the problem formed by eq. (5) and eq. (6), which is to find $(\boldsymbol{u}; p) \in \boldsymbol{\mathcal{X}} := \boldsymbol{\mathcal{V}}_D \times \boldsymbol{\mathcal{Q}}$, where $\boldsymbol{\mathcal{V}}_D$ and $\boldsymbol{\mathcal{Q}}$ are appropriate function spaces for the velocity (vectors already fulfilling the Dirichlet boundary conditions) and the pressure fields.

$$\begin{aligned} \rho_f \left(\frac{\partial \boldsymbol{u}}{\partial t}, \boldsymbol{v} \right) + \rho_f (\boldsymbol{u} \cdot \nabla \boldsymbol{u}, \boldsymbol{v}) + \mu (\nabla \boldsymbol{u}, \nabla \boldsymbol{v}) - (p, \nabla \cdot \boldsymbol{v}) &= \langle \boldsymbol{f}, \boldsymbol{v} \rangle \\ (q, \nabla \cdot \boldsymbol{u}) &= 0 \end{aligned} \quad (11)$$

for all $(\boldsymbol{v}; q)$ in $\boldsymbol{\mathcal{Y}} := \boldsymbol{\mathcal{V}}_0 \times \boldsymbol{\mathcal{Q}}$, where $\boldsymbol{\mathcal{V}}_0$ is the space of velocity-like fields that vanish on the Dirichlet boundary.

The basic strategy in the FEM is to replace the relevant (infinite-dimensional) spaces of functions above with finite dimensional counterparts in the variational version of the problem which leads to the algebraic system of equations that must be solved computationally.

Let us consider a conforming finite element partition \mathcal{T}_h of the domain Ω . For each element in the domain $\Omega_e \in \mathcal{T}_h$ we denote its diameter as h_e and we define

$h = \max \{h_e | \Omega_e \in \mathcal{T}_h\}$. With these tools it is possible to construct the finite element spaces in the usual way, as $\mathcal{X}_h = \mathcal{V}_{D,h} \times \mathcal{Q}_h$, with $\mathcal{V}_{D,h} \subset \mathcal{V}_D$, $\mathcal{Q}_h \subset \mathcal{Q}$. The finite element solution will be a function $\mathbf{U}_h = [\mathbf{u}_h, p_h] \in \mathcal{X}_h$, and since we will be using equal-order spaces for the velocity and the pressure, the solution can be expressed as (summation is assumed for repeated indices)

$$u_{h,j} = N^b U_j^b, \quad p_h = N^b P^b \quad (12)$$

for $j = 1, \dots, n_{\text{dim}}$ and $b = 1, \dots, n_{\text{nodes}}$; where the N^b are the shape functions, n_{dim} is the number of space dimensions (2 or 3) and n_{nodes} is the total number of mesh nodes.

Once the finite element discretization is defined, the problem presented in Equation (11) can be expressed using a compact notation as *find* $\mathbf{U}_h \in \mathcal{X}_h$ such that

$$\left(\mathbf{M} \frac{\partial}{\partial t} \mathbf{U}_h, \mathbf{V}_h\right) + B(\mathbf{U}_h, \mathbf{V}_h) = L(\mathbf{V}_h) \quad \forall \mathbf{V}_h \in \mathcal{X}_{h,0} \quad (13)$$

with

$$B(\mathbf{U}_h, \mathbf{V}_h) := (\mathbf{u}_h \cdot \nabla \mathbf{u}_h, \mathbf{v}_h) - (p_h, \nabla \cdot \mathbf{v}_h) + (\nabla \cdot \mathbf{u}_h, q_h) + \nu (\nabla^S(\mathbf{u}_h), \nabla \mathbf{v}_h) \quad (14)$$

$$L(\mathbf{V}_h) := (\mathbf{f}, \mathbf{v}_h) + \int_{\Gamma_N} \mathbf{t}_N \cdot \mathbf{v}_h \, d\Gamma \quad (15)$$

and

$$\mathbf{M} = \begin{bmatrix} \rho_f & 0 & 0 & 0 \\ 0 & \rho_f & 0 & 0 \\ 0 & 0 & \rho_f & 0 \\ 0 & 0 & 0 & 0 \end{bmatrix} \quad (16)$$

3.2.1 Stabilization

In the present work we want to make use of the simplest linear simplex elements, for both the pressure and velocity approximations. However, for problems of the form of eq. (13) (i.e., saddle-point problem, see [8]) not all velocity-pressure element pairs lead to viable numerical methods. A necessary condition to guarantee the stability of a particular combination is that the finite element spaces must fulfil the *inf-sup* or Ladyzhenskaya-Babusška-Brezzi (LBB) condition [8], and, in particular, the equal-order, piecewise linear spaces for the velocity and for the pressure ($\mathcal{P}_1/\mathcal{P}_1$ element) do not fulfil this condition [22]. Nonetheless, one can resort to stabilization methods to fix the numerical method resulting from the use of element pairs not fulfilling the LBB condition by modifying the weak form of the problem.

The Variational multiscale method (VMS) [25, 12] method provides a theoretical framework for the development of stabilized finite element formulations. These are based on the explicit consideration of the decomposition of the continuous solution into a part belonging to the finite element space \mathcal{X}_h and its complement in the continuous solution space $\tilde{\mathcal{X}}$, or *subscale*.

In this work we consider the algebraic sub-grid scales (ASGS) variant of VMS [13], which leads to rewriting the problem eq. (13) as *find* $\mathbf{U}_h \in \mathcal{X}_h$ such that

$$\left(\mathbf{M} \frac{\partial}{\partial t} \mathbf{U}_h, \mathbf{V}_h\right) + B_{ASGS}(\mathbf{U}_h, \mathbf{V}_h) = L_{ASGS}(\mathbf{V}_h) \quad (17)$$

where $B_{ASGS}(\mathbf{U}_h, \mathbf{V}_h)$ and $L_{ASGS}(\mathbf{V}_h)$ are computed by adding a number of stabilization terms to the analogous terms in eqs. (14) and (15), respectively. The resulting discrete problem does not suffer from the numerical instabilities that affect the Galerkin problem and allows us to work with the simplest finite element pair. A detailed derivation of the stabilized equations can be found in [10, 16].

3.3 Time integration and linearized system of equations

After assembling all the elemental contributions and imposing the boundary conditions, eq. (17) leads to a system of equations of the form

$$\mathbf{M} \begin{bmatrix} \frac{\partial \mathbf{U}}{\partial t} \\ 0 \end{bmatrix} + \mathbf{C}(\mathbf{U}, \mathbf{P}) \begin{bmatrix} \mathbf{U} \\ \mathbf{P} \end{bmatrix} = \mathbf{F} \quad (18)$$

where \mathbf{U} and \mathbf{P} stand for the nodal unknowns of the velocity and pressure respectively. For the time discretization we use a second-order Bossak time integration scheme [66], which defines the velocities as

$$\begin{bmatrix} \mathbf{U} \\ 0 \end{bmatrix}^{n+1} = \begin{bmatrix} \mathbf{U} \\ 0 \end{bmatrix}^n + \Delta t \left((1 - \gamma_N) \begin{bmatrix} \frac{\partial \mathbf{U}}{\partial t} \\ 0 \end{bmatrix}^n + \gamma_N \begin{bmatrix} \frac{\partial \mathbf{U}}{\partial t} \\ 0 \end{bmatrix}^{n+1} \right) \quad (19)$$

The Bossak method introduces a relaxation factor in the acceleration of the system in eq. (18)

$$(1 - \alpha_B) \mathbf{M} \begin{bmatrix} \frac{\partial \mathbf{U}}{\partial t} \\ 0 \end{bmatrix}^{n+1} + \alpha_B \mathbf{M} \begin{bmatrix} \frac{\partial \mathbf{U}}{\partial t} \\ 0 \end{bmatrix}^n + \mathbf{C}(\mathbf{U}^{n+1}, \mathbf{P}^{n+1}) \begin{bmatrix} \mathbf{U} \\ \mathbf{P} \end{bmatrix}^{n+1} = \mathbf{F}^{n+1} \quad (20)$$

where n is the time-step index. Combining eqs. (19) and (20) and rearranging terms one can rewrite eq. (20) in residual form as

$$\begin{aligned} \mathbf{R}(\mathbf{U}^{n+1}, \mathbf{P}^{n+1}) = & \mathbf{F} - \frac{1 - \alpha_B}{\gamma_N \Delta t} \mathbf{M} \begin{bmatrix} \mathbf{U} \\ 0 \end{bmatrix}^n + \left((1 - \alpha_B) \left(\frac{1}{\gamma_N - 1} \right) + \alpha_B \right) \mathbf{M} \begin{bmatrix} \frac{\partial \mathbf{U}}{\partial t} \\ 0 \end{bmatrix}^n + \\ & - \left(\frac{1 - \alpha_B}{\gamma_N \Delta t} \mathbf{M} + \mathbf{C} \right) \begin{bmatrix} \mathbf{U} \\ \mathbf{P} \end{bmatrix}^{n+1} \end{aligned} \quad (21)$$

where we choose $\alpha = -0.3$ and $\gamma_N = 1/2 - \alpha_B$, as this combination of parameters provides maximal damping of the highest frequencies and a robust behavior overall [66]. The nonlinearities present in eq. (5) are linearized using a first-order Taylor expansion. That is, at each nonlinear iteration i one solves

$$\mathbf{R}_{i+1}^{n+1} \approx \mathbf{R}_i^{n+1} + \left(\frac{\partial \mathbf{R}}{\partial \mathbf{U} \partial \mathbf{P}} \right)_{i+1}^{n+1} \begin{bmatrix} \delta \mathbf{U} \\ \delta \mathbf{P} \end{bmatrix}^{n+1} = 0 \quad (22)$$

Then the solution and the residual are iteratively updated with Picard's method as

$$\begin{aligned} \begin{bmatrix} \mathbf{U} \\ \mathbf{P} \end{bmatrix}_{i+1}^{n+1} &= \begin{bmatrix} \mathbf{U} \\ \mathbf{P} \end{bmatrix}_i^{n+1} + \begin{bmatrix} \delta \mathbf{U} \\ \delta \mathbf{P} \end{bmatrix}_{i+1}^{n+1} \\ \mathbf{R}_0^{n+1} &= \mathbf{R}(\mathbf{U}^n, \mathbf{P}^n) \\ \mathbf{R}_{i+1}^{n+1} &= \mathbf{R}(\mathbf{U}_i^{n+1}, \mathbf{P}_i^{n+1}) \end{aligned} \quad (23)$$

Algorithm 3 Solve Fluid solution step algorithm.

```

1:  $i \leftarrow 0$  ▷ initialize iteration index
2:  $\delta \mathbf{U}_0^{n+1}, \delta \mathbf{P}_0^{n+1} \leftarrow \text{INITIALIZEToZERO}()$ 
3:  $\mathbf{U}_0^{n+1}, \mathbf{P}_0^{n+1}, \mathbf{R}_0^{n+1} \leftarrow \text{UPDATEUNKNOWNs}(\delta \mathbf{U}_0^{n+1}, \delta \mathbf{P}_0^{n+1})$  ▷ eq. (23)
4: while  $\|\mathbf{R}_i^{n+1}\| > \text{tolerance}$  do
5:    $\delta \mathbf{U}_{i+1}^{n+1}, \delta \mathbf{P}_{i+1}^{n+1} \leftarrow \text{ASSEMBLESYSTEMANDSOLVE}(\mathbf{U}_i^{n+1}, \mathbf{P}_i^{n+1})$  ▷ eq. (25)
6:    $\mathbf{U}_{i+1}^{n+1}, \mathbf{P}_{i+1}^{n+1}, \mathbf{R}_{i+1}^{n+1} \leftarrow \text{UPDATEUNKNOWNs}(\delta \mathbf{U}_{i+1}^{n+1}, \delta \mathbf{P}_{i+1}^{n+1})$  ▷ eq. (23)
7:    $i \leftarrow i + 1$ 

```

where, in evaluating the derivative of the residual, we use the following approximation

$$\frac{\partial \mathbf{R}}{\partial \mathbf{U} \partial \mathbf{P}} \approx \frac{1 - \alpha_B}{\gamma_N \Delta t} \mathbf{M} + \mathbf{C}_i^{n+1} \quad (24)$$

where the indices are applied only to matrix \mathbf{C} , as \mathbf{M} does not depend on the solution. Note that this approximation assumes that the variation of \mathbf{C} is moderate compared to that of the solution vector itself, otherwise, convergence problems can appear. Consequently, the final system to be solved reads

$$-\left(\frac{1 - \alpha_B}{\gamma_N \Delta t} \mathbf{M} + \mathbf{C}_i^{n+1}\right) \begin{bmatrix} \delta \mathbf{U} \\ \delta \mathbf{P} \end{bmatrix}_{i+1}^{n+1} = \mathbf{R}_i^{n+1} \quad (25)$$

Algorithm 3 summarizes a schematic fluid solution step.

4 Coupling strategy

The overall PID problem involves different material components whose behavior may or may not significantly affect the others.

Specifically, the drill bit is modelled as a rigid solid whose motion is imposed. The fluid phase is modelled as explained in Section 3 and it responds to the motion of the drill bit by means of an arbitrary Lagrangian-Eulerian (ALE) strategy, which accounts for the movement of the fluid mesh. Essentially, the drill bit rotating velocity is imposed at all nodes of the fluid using a *mesh velocity* auxiliary variable, and then all the terms in eq. (17) are computed using the difference between the *velocity* unknown and the imposed *mesh velocity*. No-slip Dirichlet boundary conditions are applied at the boundaries of the fluid domain. In addition, the motion of the particles is also affected by the drill bit through contact with the DEM surfaces, which cover the drill bit walls. All these coupling relations are schematically represented in Figure 4.

While the assumption that neither the fluid nor the particles affect the drill bit is reasonable in the present context, the one-way coupled hypothesis of the fluid-particle coupling requires further study. There exist no clear-cut rules by which one can infer the applicability of the one-way only strategy, apart from perhaps the oft-cited 0.1%-volume fraction of the disperse phase [21, 40]. However, the matter is subtle due to the strong inhomogeneities that inevitably appear in the volume fraction distribution of

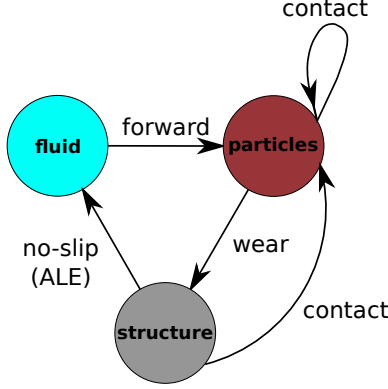


Fig. 4 *Conceptual diagram of interactions taken into account in the PID example.*

the particles; see [10]. In this work, the average volume fractions are above the 0.1% limit (it is closer to 1% on average), so a simple one-way coupling strategy cannot be justified a priori. Nonetheless, we have left this issue for future work, since we believe this simplifying assumption may be sufficiently accurate in a number of practical cases, while avoiding some of the difficulties and pitfalls (e.g., poor approximation of gradients in thin tubes, small element size-to-particle diameter ratios etc.) associated with a two-way coupled strategy.

4.1 Coupling forces

The one-way coupling considered in this work is completely determined by the terms \mathbf{F}_{coup} and \mathbf{T}_{coup} in eqs. (1) and (2). The formulation chosen here is based on the linear decomposition of several hydrodynamic effects and it is valid for a small but finite-sized particles [41]. That is, the fluid-particle coupling force is

$$\mathbf{F}_{\text{coup}} = \mathbf{F}_{\text{hydr}} + \mathbf{F}_{\text{B}} \quad (26)$$

where \mathbf{F}_{hydr} denotes the hydrodynamic force and \mathbf{F}_{B} is the buoyancy force. The latter is taken to be simply the Archimedean push due to the hydrostatic pressure alone, that is

$$\mathbf{F}_{\text{B}} = (m_p - m_f)\mathbf{g} \quad (27)$$

The hydrodynamic force is given by the following combination:

$$\mathbf{F}_{\text{hydr}} = \mathbf{F}_{\text{U}} + \mathbf{F}_{\text{A}} + \mathbf{F}_{\text{D}} + \mathbf{F}_{\text{H}} + \mathbf{F}_{\text{L}} \quad (28)$$

where \mathbf{F}_{U} stands for the unperturbed fluid force, \mathbf{F}_{A} for the added mass force, \mathbf{F}_{D} for the viscous drag force, \mathbf{F}_{H} for the viscous history force (unsteady part of the viscous drag) and \mathbf{F}_{L} is the lift force ([40]).

In order to simplify the formulation, we will neglect both F_H and F_L . F_H is expected to be small, since this force is only significant at very small Reynolds numbers and for strongly oscillatory motions [14], which are not representative of the expected (and observed) motion of the rather inertial particles and moderate levels of ambient turbulence (agitation). It is less obvious that the lift forces can in fact be neglected. Nonetheless, we have done so for the following reasons:

- No suitable lift force model for the lift in a power-law fluids is currently available
- The lift force has, for heavy particles, a much smaller magnitude than other forces, like the drag force in most turbulent regimes [65, 42] (except for particles that spend a lot of time inside the boundary layer [32]), and so it can be treated as a correction to a simpler model than neglects it, which is left for future work. This means it is likely that *neglecting this force does not alter very significantly the qualitative conclusions of this work*.

Similarly, one can consider an expression for the torque, although we will neglect its effect in this work (i.e. $T_{\text{coup}} \equiv \mathbf{0}$) for similar reasons. Next the form taken by each of the terms on the RHS of eq. (28) is discussed.

4.1.1 Unperturbed fluid and added mass forces

In the inviscid-flow limit, valid for vanishing viscosity, the equation of Auton–Hunt–Prud’Homme applies [3], which is in the form of eq. (26) (neglecting lift):

$$\mathbf{F}_{\text{hydr}} = \mathbf{F}_U + \mathbf{F}_A \quad (29)$$

F_U denotes the force that the sphere of fluid displaced by the particle would feel if taken as a point-mass. This force should correspond to its mass, m_f , multiplied by its acceleration, that is, the material acceleration of the background fluid field, as measured at the center of the sphere. Thus, this force reads

$$\mathbf{F}_U = m_f \frac{D\mathbf{u}}{Dt} \quad (30)$$

where the capitalized derivative operator denotes the material derivative. Loth [39] argues that the fact that the expression of F_U is valid in these two regimes confirms that the expression should be robust generically, and so we will assume this conclusion to be applicable in the present context as well.

Similarly, with respect to the added mass force, the following expression holds both in the inviscid and the vanishing particle Reynolds number limit,

$$\mathbf{F}_A = \frac{1}{2} m_f \left(\frac{D\mathbf{u}}{Dt} - \frac{d\mathbf{v}}{dt} \right) \quad (31)$$

Moreover, there is considerable evidence of its accuracy outside the theoretical range of validity [61, 29].

At the opposite limit (vanishing Re_p) the equation of motion is instead given by the Maxey–Riley equation (MRE) [43]. This time, the expression for the hydrodynamic force is given by

$$\mathbf{F}_{\text{hydr}} = \mathbf{F}_U + \mathbf{F}_A + \mathbf{F}_D + \mathbf{F}_H \quad (32)$$

where the forces, with the same subindices as in eq. (29), denote forces with the same physical meaning. In the MRE, both eqs. (30) and (31) are also applicable. Given that these forces are independent of the viscosity, we will assume that these expressions are valid for the complete range of Reynolds numbers too and applicable also in the context of power-law fluids.

4.1.2 Drag force

The drag force can be defined as the ensemble-averaged force experienced by a particle submerged in a statistically stationary flow in the direction of the relative velocity between the particle and the far-field averaged flow velocity. It can be expressed as

$$\mathbf{F}_D = -\frac{1}{2}A_p C_D \rho_f \|\mathbf{w}\| \mathbf{w} \quad (33)$$

where A_p is the cross-sectional area of the particle, $\mathbf{w} = \mathbf{v} - \mathbf{u}$ is the slip velocity and where the drag coefficient (C_D) is in general dependent on the Reynolds number based on the particle size (Re_p), the shape of the particle [38], the local solid fraction [7] and the properties of the fluid.

No analytical expression the drag force is available for other than some ideal cases, such as a the limit of vanishingly small Reynolds number of an incompressible, Newtonian fluid. In this case, one has the Stokes drag law, defined by $C_D = 12/Re_p$ for

$$Re_p = \frac{Wd_p}{2\nu} \quad (34)$$

where W is the magnitude of the slip velocity and ν is the kinematic viscosity. In general, one must resort to (semi-)empirical models, obtained by applying curve-fitting techniques on physical or numerical empirical data.

The literature on the hydrodynamic forces of a sphere submerged in a non-Newtonian fluid is certainly much more scarce than that for Newtonian fluids. A comprehensive review can be found in [5]. Here we employ the empirical expression proposed in [55] to predict the terminal velocity of particles in power-law fluids in the context of drilling operations. Their formulation has only been tested in stationary conditions but due to our hypothesis of the additive decomposition of the different effects, we will consider it adequate for our purposes. They provide the following expression for the empirical drag coefficient

$$C_{D,\text{Shah}} = \left(A^2 Re_p^{2B-2} \right)^{\frac{1}{2-n}} \quad (35)$$

with the empirically determined parameters

$$\begin{aligned} A &= 6.9148n^2 - 24.838n + 22.642 \\ B &= -0.5067n^2 + 1.3234n - 0.1744 \end{aligned} \quad (36)$$

and where the particle Reynolds number is defined as

$$Re_{p,Shah} = 2^{n-1} \frac{\|\mathbf{w}\|^{2-n} d_p^n}{K/\rho_f} \quad (37)$$

The model above is valid for $n \in [0.281, 1]$ and $Re_{p,Shah} \in [0.001, 1000]$. Note that using the characteristic values calculated in Section 4.2 we can check whether the conditions for the validity of this model are met. The value of n is clearly well into the range of validity. In order to estimate the characteristic values of $Re_{p,Shah}$ we can use the estimates for the mean velocity and assume a conservative value for the relative velocity based on it, say 50 % of its value. For instance, in the inlet tube area (Table 1), this estimate would yield $Re_p \approx 140$, while this number could reach $Re_{p,Shah} \approx 3000$ inside the nozzles. Again, it is expected that the maximum relative velocity occurs inside the nozzles and since the value of $Re_{p,Shah}$ is estimated to be only slightly greater than the range of validity there, we will accept the associated error nonetheless. The error associated with this choice is unknown but we do not expect it to be too large, especially when taking into account the low degree of non-Newtonian behaviour (n relatively close to one) of the mud.

4.2 Characteristic scales of the coupled problem

In order to verify the range of applicability of the different models and the level of numerical resolution required for the simulations it is important to survey the different scales involved in the problem.

4.2.1 Characteristic scales of the flow

Let us consider some characteristic scales relevant to the continuous problem. From Tables 2 and 3, one can estimate the average velocities in the different sections of the geometry. Similarly, the fluid residence time (average time spent by the fluid molecules in the domain) can be calculated by dividing the volume over the flux. These and other derived quantities relevant to the fluid are included in Table 1.

A Reynolds number can be calculated for power-law fluids, following [44], as:

$$Re_{p,PL} = \frac{2^{3-n}}{(3 + 1/n)^n} \frac{U^{2-n} d_p^n}{K/\rho_f} \quad (38)$$

who also experimentally derived the following criterion for the transition to turbulent flow in a pipe:

$$Re_{p,PL} > 2000 \quad (39)$$

According to the estimates discussed above the flow in the inner inlet tube is expected to be just on the verge of turbulence ($Re_{p,PL} \approx 4000$) and only moderately turbulent in the nozzles ($Re_{p,PL} \approx 20800$ assuming equal distribution of flow among the four nozzles). This is the maximum Reynolds number expected in the flow, as this is the most constrained section of the conduct and

$$Re_{p,PL} \sim U^{2-n} d_p^n \sim (d_p^{-2})^{2-n} d_p^n \sim d_p^{3n-4} = d_p^{-1.717} \quad (40)$$

which is monotonically decreasing. We thus expect a mostly laminar or transitional flow regime, with some areas presenting weak turbulent or transitional regimes. Relatively moderate turbulence is expected inside the nozzles.

With regards to the near-boundary resolution, one can calculate an analogue to the y^+ distance by [60]

$$y_{PL}^+ = y_{PL}^+(y) = \frac{\tau_w^{1/n-1} \rho_f}{K^{1/n}} y \quad (41)$$

where τ_w is the shear stress at the wall, which can be estimated as

$$\tau_w = \frac{1}{2} f \rho_f U^2 \quad (42)$$

and where f is the friction factor $f = 16/Re_{p,PL}$ [44]. It is interesting to calculate the distance from the wall, h^+ , at which $y_{PL}^+ = 1$, since that is the size recommended for the smallest computational cells placed close to it [36]. These values are summarized in Table 1.

Table 1 Characteristic scales

Parameter	Value	Description
Flow		
U_{inlet}	12.68 m s ⁻¹	average velocity in inlet tube
$U_{nozzles}$	156.2 m s ⁻¹	average velocity in nozzles
t_{res}	0.38 s	total domain residence time
$t_{res, internal}$	0.053 s	internal domain residence time
h_{inlet}^+	2.8×10^{-4} m	recommended size of computational cell adjacent to the wall (inlet tube)
$h_{nozzles}^+$	1.8×10^{-5} m	recommended size computational cell adjacent to the wall (nozzles)
Particles parameters		
d_p	0.001 981 2 m	diameter of steel particles
ρ_p	7850 kg/m ³	density of steel particles
Mixed parameters		
α_p	0.021	solid volume fraction
$\alpha_{p,\rho}$	0.128	solid mass fraction
Operation conditions		
Q	0.029 02 m ³ /s	fluid flux
N_{inlet}	1.5×10^5 s ⁻¹	number of particles flux
Ω_{drill}	-2π s ⁻¹	angular velocity of drill-bit

4.2.2 Characteristic scales of the particles

The Stokes number is a nondimensional measure of the particle inertia. It is defined as the quotient between the particle's relaxation time (a characteristic time that it takes the fluid to slow down the relative motion of the particle) and the typical time scale of the background flow fluctuations, T . For instance, in the range of applicability of the MRE, the relaxation time is conventionally defined as the time taken by the particle to be slowed down by the fluid to $1/e$ of its initial velocity. Using the MRE (and neglecting F_H) the Stokes number can be calculated as

$$St = \frac{2\rho + 1}{36} \frac{d_p^2}{\nu} \frac{1}{T} \quad (43)$$

where $\rho = \rho_p/\rho_f$. For this particular case, the relaxation time does not depend on the initial relative velocity (the relaxation time is a constant). This is not strictly true for our model, although this notion of a characteristic value for the Stokes number is still a useful notion.

In Figure 5 the relaxation times for the steel particles are shown as numerically calculated for different initial relative velocities. The range of values covers all the values of interest in the domain and however the relaxation time is seen to remain quite stable around 0.003 s. This time scale can thus be used as a reference relaxation time in what follows.

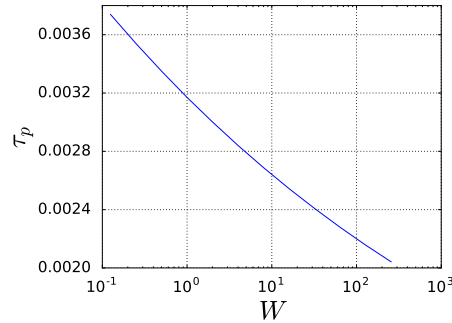


Fig. 5 Relaxation times for different initial relative velocities obtained numerically using the drag model of Shah.

The Stokes number can be used to distinguish particulate flow regimes, classifying them into ballistic ($St > 1$) and tracer-like ($St < 1$) with respect to the fluid motion associated with the time scale T . When St is much greater than one, it is normally assumed that the particles do not have time to respond to the fluid dynamics, see for example the discussion in [6]. In order to estimate the importance of an accurate description of the turbulent structures, it is therefore useful to look at the Stokes number.

For instance, we have seen that inside the nozzles we expect to find the most intense turbulence. But since the particles move at about 100 m s^{-1} there, they only spend less than $1 \times 10^{-3} \text{ s}$ in them. This means that $St > 3$ and most likely $St \gg 3$, as the typical turbulent fluctuations will be significantly smaller spacial amplitude than the length of

the nozzles. This means that it is mostly the mean flow that will dictate the trajectory of the particles inside the nozzles. Note however that this is true *as long as the drag force is the dominating hydrodynamic force*. We will come back to this question in Section 5.

4.2.3 Characteristic scales related to the interactions

In order to assess the importance of the influence of the particle in the flow, the most important scale is the typical solid fraction, which is the global proportion of particles volume to fluid volume [18]. Another interesting quantity is the solid mass fraction $\alpha_{p,\rho}$ that takes into account the different densities of the two phases. These quantities can be preliminarily estimated assuming a homogeneous distribution of particles as

$$\begin{aligned}\alpha_p &= N_{\text{inlet}} \frac{V_p}{Q} \\ \alpha_{p,\rho} &= \frac{\rho_p}{\rho_f} \alpha_p\end{aligned}\tag{44}$$

where N_{inlet} is the number of particles entering the domain per second, $V_p = \frac{1}{6}\pi d_p^3$ is the volume of one steel ball and Q is the fluid inlet flux. The characteristic values for the present problem can be found in Table 1.

4.3 Overall algorithm

Given that the DEM phase has a much stricter time step requirements than the fluid, due to the very small time scales associated to the contact dynamics that it resolves, we employ a sub-stepping scheme so that, for every fluid time step, many DEM time steps are performed. The fluid is advanced first, and then the DEM catches up in smaller time step increments. The fluid field quantities are evaluated at every DEM step too taking a weighted average between old and new fluid values. The pseudo-code is shown in Algorithm 4, where $N_{f,\text{steps}}$ refers to the total number of fluid time steps in the simulation and where t_{DEM} keeps track of the time for the DEM phase. The code implementation was done within the framework Kratos Multiphysics [20].

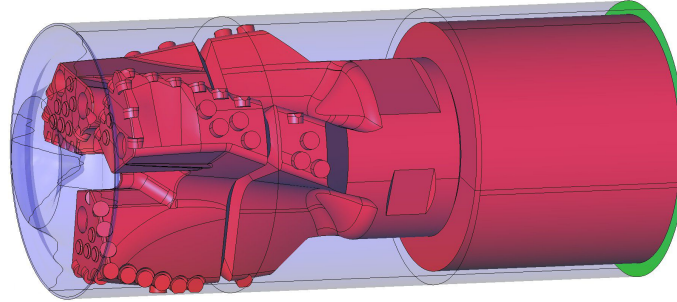
5 PID Simulations

5.1 Domain geometry

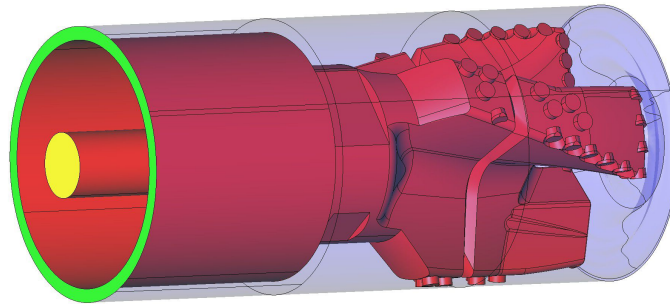
The geometry of the drill-bit and the surfaces defining the rocky bed and casing are shown in Figure 6. The surfaces in red belong to the rotating part of the domain, while the casing and ground surfaces are shown in a transparent blue. The inlet surface, at which the inlet flow condition is imposed is marked yellow, while the outlet surface (imposed normal traction) is marked in light green. In Table 2 we summarize several useful measurements derived from the geometry.

5.2 Parameters

The values that have been kept fixed throughout this study are summarized in Table 3.



bottom-up view



top-down view

Fig. 6 Depiction of the PID domain geometry.

Table 2 Geometric measurements

Parameter	Value	Description
D_{inlet}	0.053 975 m	interior diameter of inner tube
D_{nozzle}	0.007 69 m	interior diameter of nozzles
L_{nozzle}	0.086 m	average length of the nozzles
V_{total}	0.0111 m^3	total fluid domain considered
V_{internal}	$0.001 53 \text{ m}^3$	fluid of internal domain (between inlet surface and tip of nozzles)

Algorithm 4 One-way-coupled two-phase algorithm.

1: $t \leftarrow 0.0$		▷ initialize fluid
2: $n \leftarrow 0$		▷ fluid step index
3: $\mathbb{U}^0, \mathbb{P}^0 \leftarrow \mathbb{U}_{\text{init}}, \mathbb{P}_{\text{init}}$		
4: $t_{\text{DEM}} \leftarrow 0.0$		▷ initialize DEM
5: $m \leftarrow 0$		▷ DEM step index
6: INITIALIZEPARTICLES()		
7: SEARCHNEIGHBORS()		
8: for n in $[0, N_{f,\text{steps}}]$ do		▷ fluid solution loop
9: $t_{\text{DEM}} \leftarrow t$		
10: $t \leftarrow t + \Delta t$		▷ fluid time is advanced first
11: $n \leftarrow n + 1$		
12: ROTATEMESH(t, n)		▷ impose fluid mesh rotation
13: SOLVEFLUID(t, n)		▷ Algorithm 3
14: RECOVERDERIVATIVES()		▷ [10]
15: while $t_{\text{DEM}} < t$ do		▷ DEM sub-stepping
16: $t_{\text{DEM}} \leftarrow t_{\text{DEM}} + \Delta t_{\text{DEM}}$		
17: $m \leftarrow m + 1$		
18: LOCATEPARTICLESINFLUID()		
19: INTERPOLATEFLUIDVALUES()		
20: SOLVEDEM(t_{DEM}, m)		▷ Algorithm 2

Table 3 Physical parameters considered in this work

Parameter	Value	Description
Fluid parameters		
ρ_f	1294 kg/m ³	density of fluid
n	0.761	flow behaviour index
K	1.24 Pa s ^{0.761}	flow consistency index
Particles parameters		
d_p	0.001 981 2 m	diameter of steel particles
ρ_p	7850 kg/m ³	density of steel particles
Operation conditions		
Q	0.029 02 m ³ /s	fluid flux
N_{inlet}	$1.5 \times 10^5 \text{ s}^{-1}$	number of particles flux
Ω_{drill}	$-2 \pi \text{ s}^{-1}$	angular velocity of drill-bit

5.3 Standard settings

Parameters. For the simulations we fix a number of parameters and options that we summarize in Table 4. These settings correspond to the *standard case* (SC), and can be

considered the default parameters. We will emphasize only the values of the parameters that deviate from those in the SC to distinguish between different cases.

Table 4 Input parameters for the standard case run

Parameter	Value		Description
Coupling Parameters			
ξ_U	1		Include F_U and F_A (0 or 1)
Contact parameters			
$\mu_{p,w}$	0.42		particle-wall friction coefficient
COR	0.6		coefficient of normal restitution
ξ_C	1		compute inter-particle contact (0 or 1)
Numerical Parameters			
	internal	total	
h	0.0026 m	0.004 m	max. element size of irregular mesh ¹
$h_{\text{wall}}/h_{\text{nozzles}}^+$	1.1	27	normalized width of elements adjacent to nozzle walls
Δt	1.0×10^{-4} s	1.0×10^{-4} s	time step for the fluid-phase
δt	5×10^{-7} s	1.9×10^{-7} s	time step for the particles-phase

Boundary conditions. The boundary conditions imposed in all cases are a combination of strongly-imposed velocity conditions (uniform inlet velocity at the inlets and no-slip at the walls) and weakly imposed Neumann condition at the outlets (zero normal traction).

5.4 Internal flow results

We have run the standard internal flow simulations for a simulated time of 0.3 s. This corresponds to more than five times the residence time of the internal subdomain.

Figure 7 shows a snapshot of the particles phase with different vectorial results represented. Note the ≈ 50 -fold ratio of the largest hydrodynamic force over the largest drag force, due to the contributions of F_U and F_A around the entrance to the nozzles, where the local fluid acceleration becomes very large.

Figure 8 shows the velocity modulus contour maps on several cross-sections. Note the regularity of the flow in the inlet tube, where the Reynolds number is on the verge

¹This number is only an estimation and is used by the mesh generator (advancing front) in [15] to build the mesh.

of turbulence. Note also the rotation-triggered vortices inside the three branches of the distribution chamber both in the horizontal and vertical directions.

Figures 9a and 9b show two sets of streamlines at a particular time step. Figure 9a shows a uniformly distributed selection of streamlines that passing through equally spaced points along the inlet tube cross-section. Figure 9b shows a detail of streamlines passing through a segment of points inside a bisecting plane of one of the three branches of the distribution chamber. This figure highlights the convoluted direction of the flow in this recirculation zone.

Similarly, Figures 9c and 9d show a number of particles trajectories in the interval 0.25 s to 0.3 s. Figure 9d shows a detail where the particle temporary trapping in the recirculation zone is highlighted.

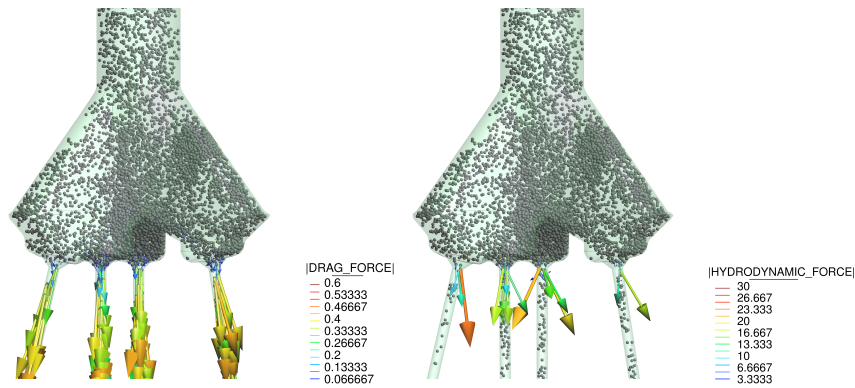


Fig. 7 Particles flowing under the action of the flow at $t = 0.25$ s. The drag force and total hydrodynamic forces are shown.

5.5 Total flow results

The total flow cases have been run for a simulated time of 0.38 s, the concentration time of the domain. In this case the mesh is slightly coarser than in the internal case for the inner tube as the focus is placed on the annulus flow.

Figure 10 shows a sequence of three snapshots where the z -component of the velocity is indicated with color on the particles surface. Significant inhomogeneities exist in the solid concentration, which indicates the need for further research to study this effect. Note that the particle size has been exaggerated by a factor 2.5 to facilitate observing them.

Figure 11 shows the contour plot of the velocity for a series of transversal and vertical cuts. Note that the velocities in the internal flow are above the maximum of 8 m s^{-1} in large parts of the domain in (Figures 11a and 11b).

In Figure 12 a sequence of contour plots of the level of wear on the rock bed is shown, demonstrating the potential for this approach to help in assessing the performance of

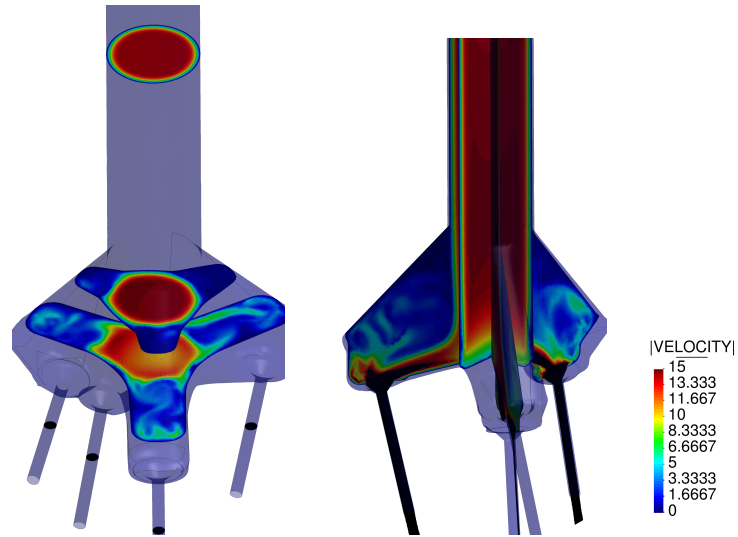


Fig. 8 Modulus of the velocity field at $t = 0.25$ s.

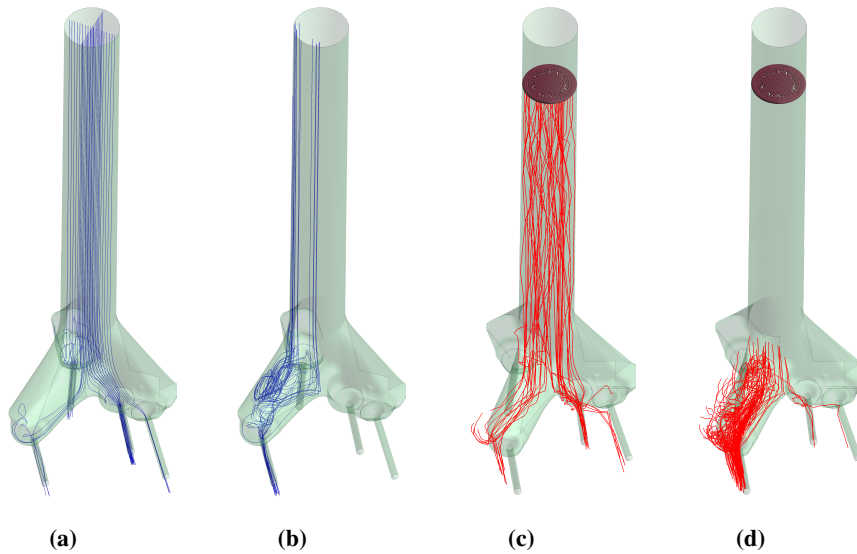


Fig. 9 Fluid streamlines at $t = 0.25$ s (a,b). Uniformly distributed streamlines (a) and detail of streamlines inside a vortical region (b). Particle trajectories for the interval 0.25 s to 0.3 s (c,d). Randomly chosen spheres (c), detail of spheres inside a vortical region (d).

changes in the design or the operation conditions. The action of the individual jets is clearly visible.

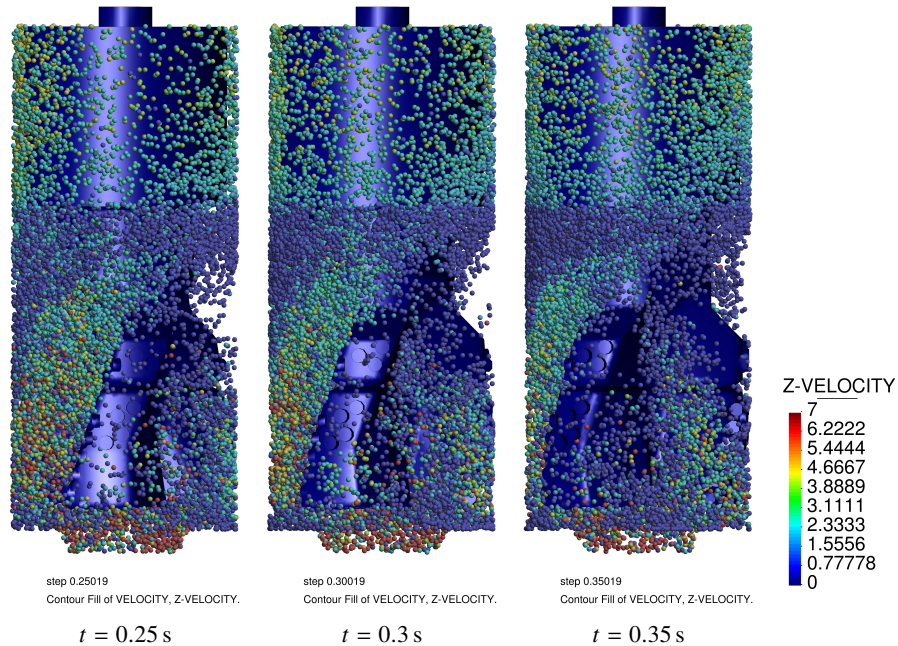


Fig. 10 Sequence of snapshots of the particles flowing under the action of the flow at different times. The colors indicate the z-component of the velocity. The size of the particles has been enlarged by 250% to facilitate visualization.

5.6 Sensitivity analyses

Given the uncertainty in the model parameters, it is interesting to investigate the influence of a few of them separately. This should help in concentrating the research efforts toward the most critical effects.

Coefficient of friction. We have investigated the effect of the coefficient of friction in the contact dynamics of the particles, but we realized that it is very weak, and no clear trend could be observed. This can be explained in terms of the fact that the prevalent regime is on impact regime, where the particles are mostly bouncing off each other and off the surfaces, rather than rubbing against each other. It is known that the friction coefficient has a strong incidence on the angle of rebound in individual impacts [57]. However, this does not seem to bear any strong effect on the dynamics of the particles as a whole, probably due to the randomized character of the collective dynamics.

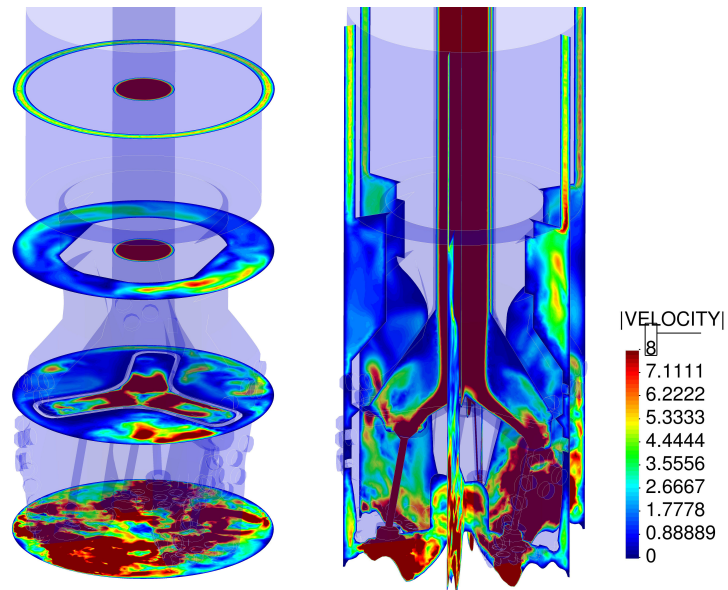


Fig. 11 Modulus of the velocity field at $t = 0.35$ s.

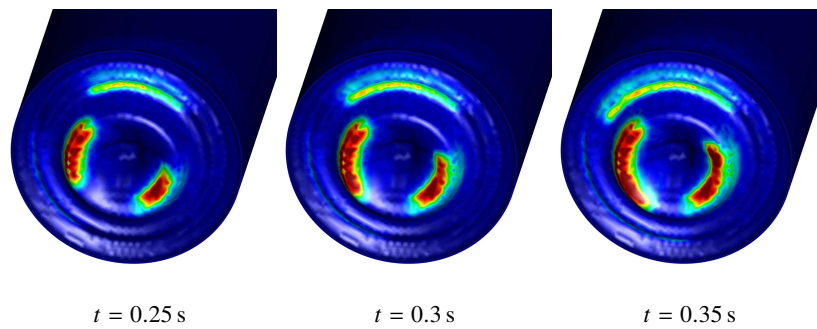


Fig. 12 Sequence of snapshots of the wear spread pattern evolution on the bed surface (red: intense wear; blue: light wear).

Coefficient of normal restitution. The coefficient of normal restitution was also studied and, in this case, a relevant effect was observed. In Figure 13 snapshots of the velocity field taken at the same time steps are compared between simulations that only differ in the COR used. The central figure corresponds to the SC, with $COR = 0.6$, while Figure 13a and Figure 13c correspond to $COR = 0.2$ (highly dissipative) and $COR = 0.8$ (highly elastic). Clearly, the most dissipative case flows much more easily as the particles concentrate near the path of the dominating streamlines into the nozzles. When the COR is raised, the particles tend to occupy more space and accumulate more, as the number of particles in the domain goes from 8759 (close to the value of 7850 calculated by multiplying the input α_p by the domain volume) for the most dissipative case, to 12 469 for the mildly dissipative case. This represents a 42 % increase after only a quarter of a turn of the drill bit. Also, looking at Figure 14, the larger accumulation of particles that appears with a higher COR leads to a more clear concentration of the wear pattern near the entrance of the nozzles. Therefore, given the importance of the COR, and since, in spite of what is commonly assumed in practice, it is known that the COR is in fact not independent of the velocity [34], we must conclude that more work is needed to characterize the contact with higher accuracy, especially given the large range of characteristic velocities for different regions of the domain.

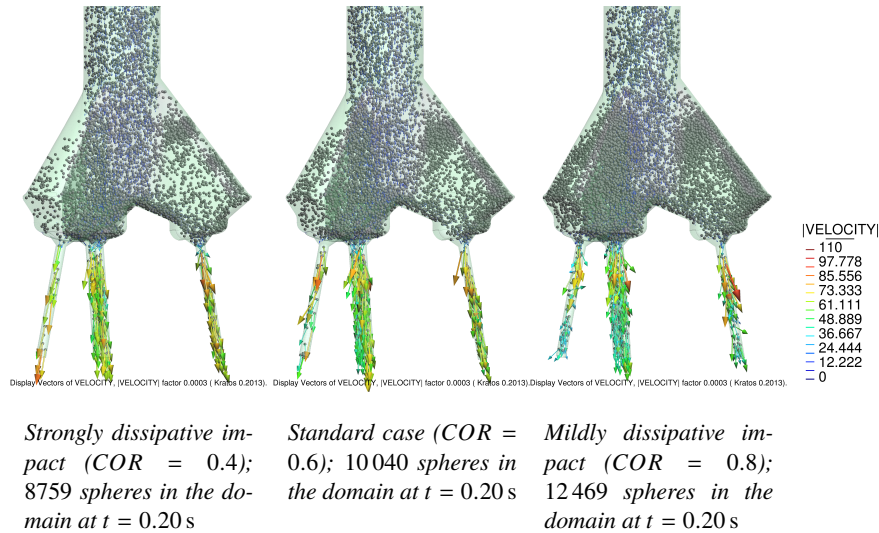


Fig. 13 Effect of variations in the coefficient of normal restitution (red: intense wear; blue: light wear).

5.7 An attempt to simplify the problem

Given the complexity of the simulations of PID operations, it is interesting to look for simplifying assumptions that can be made in order to reduce the computational cost per simulation, or limit the number of parameters to be considered in the sensitivity analyses. We have looked at two different possibilities:

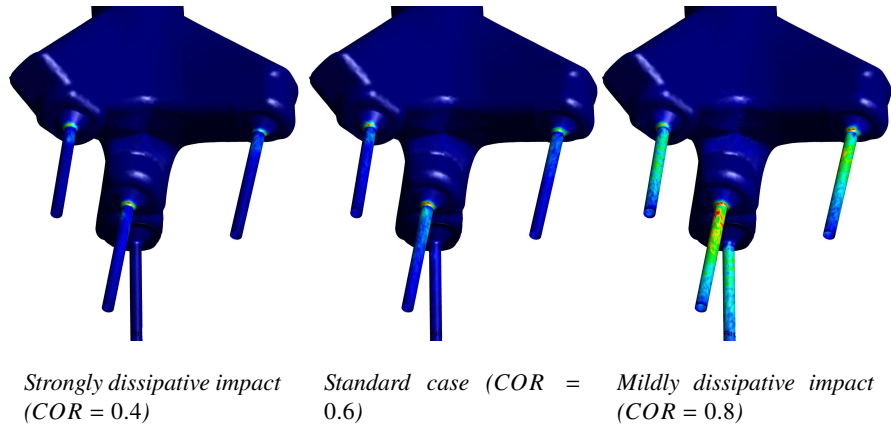


Fig. 14 Effect of variations in the coefficient of normal restitution on the wear pattern (red: intense wear; blue: light wear).

Effect of neglecting inter-particle contacts. We have investigated the importance of considering inter-particle contacts, since it would greatly simplify the analysis if we could do without them at all in the following ways:

1. The computational cost would be greatly reduced, thanks to avoiding the most expensive parts of the DEM algorithm (force calculation and search).
2. The parameter space would be reduced, since only the particle-wall contact parameters would matter.
3. It would be possible to alter (increase) the given concentration of particles to speed up the simulations, since each particle could be seen as an independent statistical test.

Figure 15 shows that neglecting inter-particle forces is not possible, at least at the current value of α_p . When no interactions are used, the flow becomes more chaotic as the particles do not become entrained in the general flow towards the nozzles. Therefore, there is an increased rate of accumulation. Since the rate of inter-particle momentum transfer is null, slow particles trapped in the recirculation region tend to remain there for longer times, increasing the particles concentration artificially.

Pseudo-steady-state solution. We have also considered the possibility of simplifying the problem by averaging the fluid field over a short time interval, and taking the averaged field as the fluid field for the computations with particles. In order to obtain the average field, the fluid-only simulation was run passed the initial transient phase and averaged over a time interval (correcting for the rotation, of course) considered sufficient to smooth out all the transients. Specifically, our criterion was to average at least for a period equivalent to half the residence time of the flow. Figure 16 shows contour plots comparing the velocity field for a single snapshot for the SC with the average field at

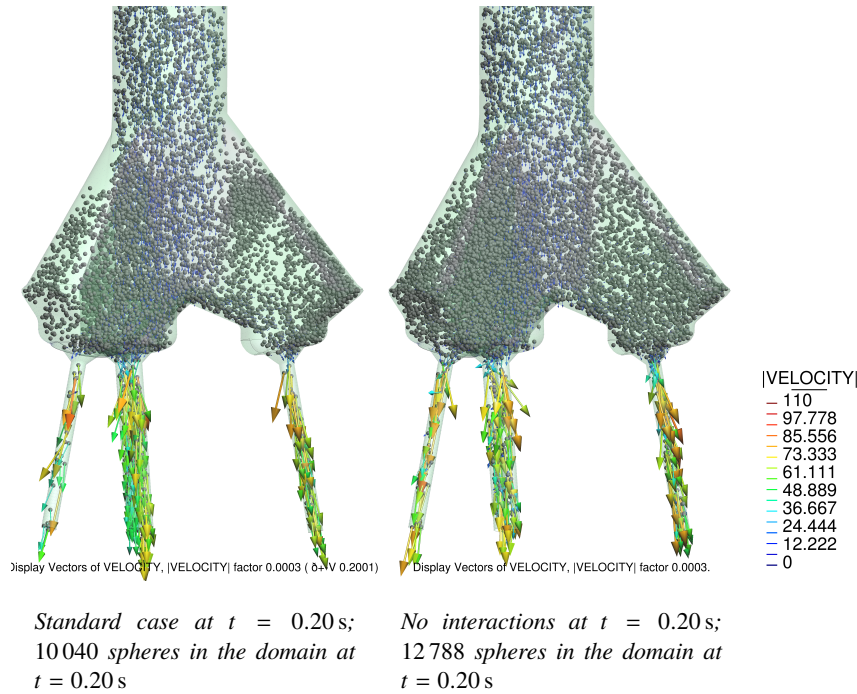


Fig. 15 Effect of inter-particle interactions on the particles movement

the same instant. Note that the average field is only rotated with the drill bit, but does not change relative to that solid-body motion.

Apparently, the large-scale characteristics of the flow are approximately well captured. However, we have found that this strategy (on its own) completely fails when the particles are taken into account. The main reason for this seems to be that the strong fluid accelerations around the entrance to the nozzles, when averaged over time, create zones of low pressure that act as particle traps. When the flow is dynamic, these low pressure pockets are unstable with the material acceleration changing vigorously in time, so that no trapping occurs. Instead, for the averaged field, these regions act as stable attractors to the particles, creating plugs.

5.8 Measuring particle fluxes

In this section we show results corresponding to an alternative geometry. Its design is shown in Figure 17. Here the objective was to design a way to properly monitor any difference in the performance of each of the nozzles. We designed a variant of the usual DEM rigid walls of analytic type (Section 2.4). The surfaces keep the information about all the particles that cross them, their velocity and possibly other data, storing it all in a single HDF5 file for later analysis.

Figure 18 shows the resulting measurements for the nozzle surfaces shown in Figure 17b. The method allows to monitor the performance of the nozzles, tracking both

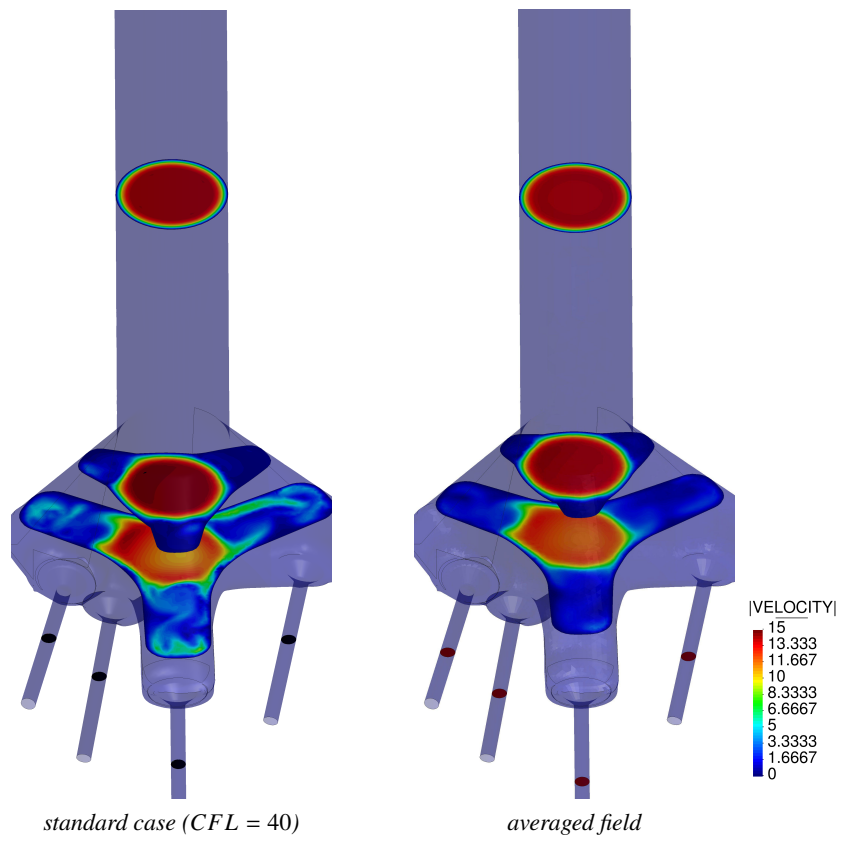


Fig. 16 Comparison of the modulus of the velocity field between the standard case at $t = 0.25$ s and the pseudo-steady field averaged velocities.

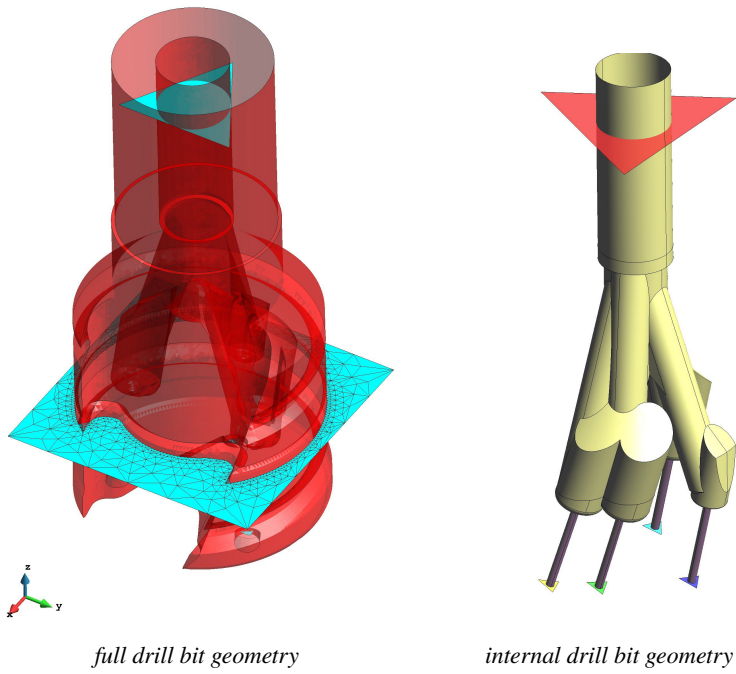


Fig. 17 Geometries of the PID drill bit with showing the flux measuring surfaces. The surfaces are triangulations that can adapt to contours as in the left picture.

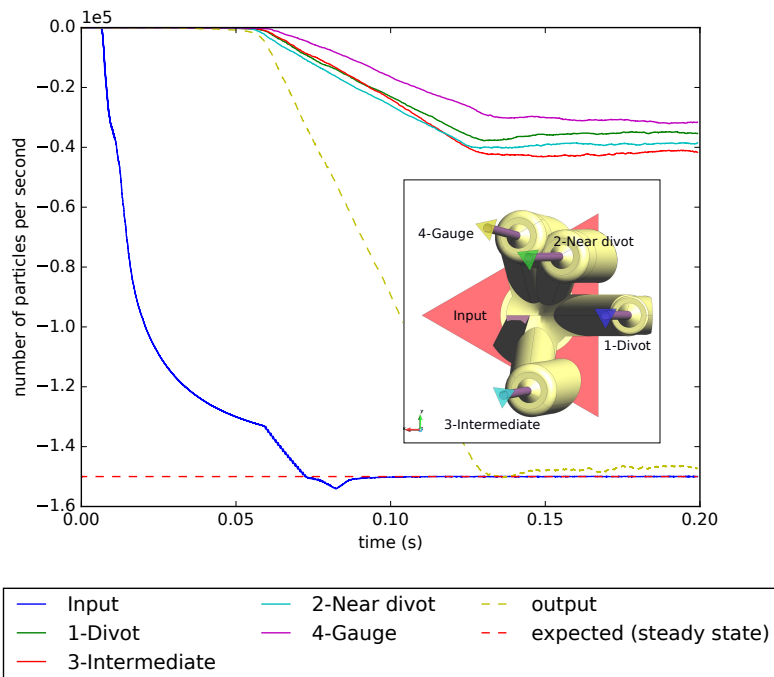


Fig. 18 Flux of particles through nozzles calculated with a moving average with an averaging interval of 0.07 s. The 'output' refers to the sum of the fluxes through the nozzles, while the expected flux corresponds to the rate of injection of particles $1.5 \times 10^5 \text{ s}^{-1}$. The sign of the measurements corresponds to the particular orientation of the normals that define the measuring surfaces, which are all opposite to the sense of the main fluid flow. The insert identifies the flux-measuring surfaces in a bottom-up perspective.

velocity and mass. Here we only show the number of particles per second that pass through each of the nozzles, identified by the labels shown in the insert of the same figure. The simulation was run for some time until the averages looked stable enough. Clearly, there are important differences in performance between the different nozzles. This type of result is a very good candidate for future validation, as the flux measurements can be obtained through experiments. Unfortunately, no data was available to us at the moment of writing this work, and such validation is left for the future.

6 Conclusions

We have described a numerical strategy for the simulation of PID operations based on a simple one-way coupled strategy. We have presented a number of arguments in support of our modelling choices and reported practical tips that we expect can help future attempts to tackle this complex problem in practice. We have also demonstrated the possibilities of the technology by highlighting how a number of effects of relevance to the design of PID drill bits can be analysed for real geometries in operational conditions and in a manageable amount of time.

Some of the the possible applications of our numerical method include

- The depiction of the internal flow of particles, including their distribution among the several pipes.
- The prediction of wear concentrations, which can be used to assess the durability of PID bit designs.
- The study of the return flow patterns, which can help to understand the movement of particles and possible sources of clogging or undesired accumulation.
- The study of the sensitivity of the system to changes in the number of particles and their granulometry.

Our analysis suggests possible reductions in the parameter space, such as the elimination of the friction coefficient as a relevant parameter. It also highlights the importance of other parameters like the COR, which should be determined with adequate precision in order to build a sufficiently accurate numerical tool. The same analysis highlights the need for further research to determine the validity of our simplified coupling scheme, and in particular:

- Extending the validity of the drag law by Shah for larger Reynolds numbers and testing it in instationary settings.
- Studying the importance of lift.
- Studying the effects of a more a sophisticated strategy that includes backward coupling, since the suspension is not lean enough to neglect the influence of the particles on the fluid phase a priori.

The last of the items above is particularly relevant, since it constitutes a big simplification, especially in cases where the particles accumulate, as well as in narrow areas where the volume of each particle cannot be neglected in principle. Such a strategy is possible and is the subject of current work by the authors. Nonetheless, it is not without difficulties:

- A two-way coupled strategy requires the use of spatially-filtered fluid equations, introducing a measure of complexity that would certainly impact the practicality of the methodology.
- The filtering techniques that are necessary to construct the fluid fraction and related fields onto the fluid mesh (and that are used implicitly in deriving the underlying theory) typically require the use of fluid elements that are significantly larger than the particles, which is difficult to ensure in many areas of the problem studied, and they become significantly less accurate near the boundaries [52, 24] (of which there are plenty around the narrow passages through which the fluid is forced).
- The availability of CFD codes capable of such problem and of engineers with the necessary knowledge in the computational field is much more scarce.

In any case, in future work we plan to compare the results from the one-way and the two-way coupled methods and analyse the sensitivity of their relationship to changes in the parameters of the problem, such as the volume fractions.

Acknowledgments

We acknowledge the financial support to CIMNE via the CERCA Programme / Generalitat de Catalunya, and also that provided by the Spanish Ministry of Economy and Competitiveness, through the “Severo Ochoa Programme for Centres of Excellence in R&D” (CEX2018-000797-S). **RAJU: WE NEED ACKNOWLEDGEMENTS**

References

- [1] Alicia Aguilar-Corona, Roberto Zenit, and Olivier Masbernat. Collisions in a liquid fluidized bed. *International journal of multiphase flow*, 37(7):695–705, 2011.
- [2] D. Antypov and J. A. Elliott. On an analytical solution for the damped Hertzian spring. *EPL (Europhysics Letters)*, 94(5):50004, jun 2011.
- [3] T. R. Auton, J. C. R. Hunt, and M. Prud’Homme. The force exerted on a body in inviscid unsteady non-uniform rotational flow. *Journal of Fluid Mechanics*, 197(-1):241, dec 1988.
- [4] Orlando Ayala, Wojciech W. Grabowski, and Lian Ping Wang. A hybrid approach for simulating turbulent collisions of hydrodynamically-interacting particles. *Journal of Computational Physics*, 225(1):51–73, 2007.

- [5] Jalel Azaiez. Bubbles, drops and particles in non-newtonian fluids. R. P. Chhabra. *The Canadian Journal of Chemical Engineering*, 85(2):251–252, may 2008.
- [6] S Balachandar. A scaling analysis for point–particle approaches to turbulent multiphase flows. *International Journal of Multiphase Flow*, 35(9):801–810, sep 2009.
- [7] R. Beetstra, M. A. van der Hoef, and J. A. M. Kuipers. Drag force of intermediate Reynolds number flow past mono- and bidisperse arrays of spheres. *AICHE Journal*, 53(2):489–501, feb 2007.
- [8] Daniele Boffi, Franco Brezzi, Michel Fortin, et al. *Mixed finite element methods and applications*, volume 44. Springer, 2013.
- [9] Guillermo Casas, Debanjan Mukherjee, Miguel Angel Celigueta, Tarek I. Zohdi, and Eugenio Onate. A modular, partitioned, discrete element framework for industrial grain distribution systems with rotating machinery. *Computational Particle Mechanics*, 4(2):181–198, apr 2017.
- [10] Guillermo Casas González. *Numerical analysis of particle-laden flows with the finite element method*. PhD thesis, Universitat Politècnica de Catalunya, 2018.
- [11] Paul W Cleary. Large scale industrial dem modelling. *Engineering Computations*, 2004.
- [12] Ramon Codina. A stabilized finite element method for generalized stationary incompressible flows. *Computer Methods in Applied Mechanics and Engineering*, 190(20-21):2681–2706, feb 2001.
- [13] Ramon Codina, Santiago Badia, Joan Baiges, and Javier Principe. Variational multiscale methods in computational fluid dynamics. *Encyclopedia of Computational Mechanics Second Edition*, pages 1–28, 2018.
- [14] CFM Coimbra and RH Rangel. Spherical particle motion in harmonic stokes flows. *AIAA journal*, 39(9):1673–1682, 2001.
- [15] J. Coll, A. and Ribó, R. and Pasenau, M. and Escolano, E. and Perez, J.Suit. and Melendo, A. and Monros, A. and Gárate. GiD v.13 Reference Manual. *CIMNE*, 2016.
- [16] Jordi Cotela-Dalmau. *Applications of turbulence modelling in civil engineering*. PhD thesis, Universitat Politècnica de Catalunya, dec 2016.
- [17] Philippe Coussot, F Bertrand, and B Herzhaft. Rheological behavior of drilling muds, characterization using mri visualization. *Oil & gas science and technology*, 59(1):23–29, 2004.
- [18] Clayton Crowe, John Schwarzkopf, Martin Sommerfeld, and Yutaka Tsuji. *Multiphase Flows with Droplets and Particles*. CRC press, 2012.

- [19] Meng Cui, Ying-hu Zhai, and Guo-dong Ji. Experimental study of rock breaking effect of steel particles. *Journal of Hydrodynamics, Ser. B*, 23(2):241–246, apr 2011.
- [20] Pooyan Dadvand, Riccardo Rossi, and Eugenio Oñate. An Object-oriented Environment for Developing Finite Element Codes for Multi-disciplinary Applications. *Archives of Computational Methods in Engineering*, 17(3):253–297, sep 2010.
- [21] OA Druzhinin and S Elghobashi. Direct numerical simulations of bubble-laden turbulent flows using the two-fluid formulation. *Physics of Fluids*, 10(3):685–697, 1998.
- [22] Alexandre Ern and Jean-Luc Guermond. *Theory and Practice of Finite Elements*, volume 159 of *Applied Mathematical Sciences*. Springer New York, New York, NY, 2004.
- [23] Yu Guo and Jennifer Sinclair Curtis. Discrete Element Method Simulations for Complex Granular Flows. *Annual Review of Fluid Mechanics*, 47(1):21–46, 2015.
- [24] Prashant Gupta, J Sun, and JY Ooi. Dem-cfd simulation of a dense fluidized bed: wall boundary and particle size effects. *Powder technology*, 293:37–47, 2016.
- [25] Thomas J.R. Hughes. Multiscale phenomena: Green’s functions, the Dirichlet-to-Neumann formulation, subgrid scale models, bubbles and the origins of stabilized methods. *Computer Methods in Applied Mechanics and Engineering*, 127(1-4):387–401, nov 1995.
- [26] Martin James and Samriddhi Sankar Ray. How Violent are the Collisions of Different Sized Droplets in a Turbulent Flow? pages 1–11, mar 2016.
- [27] Zhao Jian and Xu Yiji. The technical development for increasing rop with particle impact drilling in china. *Advanced Materials Research*, (904), 2014.
- [28] Zhao Jian, Xu Yiji, Ren Jianhua, and Hou Deju. Numerical simulation of the bottom hole flow field of particle impact drilling. 8(2):18–23, 2014.
- [29] Abdullah Abbas Kendoush, Abbas H. Sulaymon, and Sawsan A.M. Mohammed. Experimental evaluation of the virtual mass of two solid spheres accelerating in fluids. *Experimental Thermal and Fluid Science*, 31(7):813–823, jul 2007.
- [30] Harald Kruggel-Emden, M Sturm, Siegmund Wirtz, and Viktor Scherer. Selection of an appropriate time integration scheme for the discrete element method (dem). *Computers & Chemical Engineering*, 32(10):2263–2279, 2008.
- [31] Johannes GM Kuerten. Point-particle dns and les of particle-laden turbulent flow-a state-of-the-art review. *Flow, turbulence and combustion*, 97(3):689–713, 2016.
- [32] Jana Lataste, Daniel Huilier, Henri Burnage, and Jan Bednář. On the shear lift force acting on heavy particles in a turbulent boundary layer. *Atmospheric Environment*, 34(23):3963–3971, 2000.

- [33] Roy Lichtenheldt. A stable, implicit time integration scheme for discrete element method and contact problems in dynamics. In *PARTICLES V: proceedings of the V International Conference on Particle-Based Methods: fundamentals and applications*, pages 297–308. CIMNE, 2017.
- [34] J.M. Lifshitz and H. Kolsky. Some experiments on anelastic rebound. *Journal of the Mechanics and Physics of Solids*, 12(1):35–43, feb 1964.
- [35] Ji Guodong Wang Haige Wang Lingbi and Cui Meng Cheng Rongchao. Numerical simulation research on the bit nozzle flow field of particle impact drilling. *China Petroleum Machinery*, (10):6, 2012.
- [36] Rainald Löhner. *Applied Computational Fluid Dynamics Techniques*. John Wiley & Sons, Ltd, Chichester, UK, mar 2008.
- [37] Ron LORD. Bit technology keeps pace with operator activity. *World oil*, 227(11), 2006.
- [38] E. Loth. Drag of non-spherical solid particles of regular and irregular shape. *Powder Technology*, 182(3):342–353, 2008.
- [39] E. Loth. Lift of a Spherical Particle Subject to Vorticity and/or Spin. *AIAA Journal*, 46(4):801–809, apr 2008.
- [40] E Loth. Particles, drops and bubbles: Fluid dynamics and numerical methods, 2010.
- [41] E. Loth and A. J. Dorgan. An equation of motion for particles of finite Reynolds number and size. *Environmental Fluid Mechanics*, 9(2):187–206, apr 2009.
- [42] Cristian Marchioli, Maurizio Picciotto, and Alfredo Soldati. Influence of gravity and lift on particle velocity statistics and transfer rates in turbulent vertical channel flow. *International Journal of Multiphase Flow*, 33(3):227–251, 2007.
- [43] Martin R Maxey. Equation of motion for a small rigid sphere in a nonuniform flow. *Physics of Fluids*, 26(4):883—889, 1983.
- [44] A. B. Metzner and J. C. Reed. Flow of non-newtonian fluids—correlation of the laminar, transition, and turbulent-flow regions. *AIChE Journal*, 1(4):434–440, dec 1955.
- [45] Catherine O’Sullivan and Jonathan D Bray. Selecting a suitable time step for discrete element simulations that use the central difference time integration scheme. *Engineering Computations*, 2004.
- [46] J. T. Padding and A. A. Louis. Hydrodynamic interactions and Brownian forces in colloidal suspensions: Coarse-graining over time and length scales. *Physical Review E - Statistical, Nonlinear, and Soft Matter Physics*, 74(3):1–31, 2006.
- [47] Nina M Rach. Particle-impact drilling blasts away hard rock. *Oil & gas journal*, 105(6), 2007.

- [48] Rosa Ramírez, Thorsten Pöschel, Nikolai V. Brilliantov, and Thomas Schwager. Coefficient of restitution of colliding viscoelastic spheres. *Physical Review E*, 60(4):4465–4472, oct 1999.
- [49] Fu Shen Ren, Ruo Xu Ma, and Xiao Ze Cheng. Simulation of particle impact drilling nozzles based on fluent. *Advanced Materials Research*, 988:475–478, jul 2014.
- [50] Derek C Richardson, Kevin J Walsh, Naomi Murdoch, and Patrick Michel. Numerical simulations of granular dynamics: I. hard-sphere discrete element method and tests. *Icarus*, 212(1):427–437, 2011.
- [51] B. Rosa, L.-P. Wang, M.R. Maxey, and W.W. Grabowski. An accurate and efficient method for treating aerodynamic interactions of cloud droplets. *Journal of Computational Physics*, 230(22):8109–8133, sep 2011.
- [52] Pierre Sagaut. *Large eddy simulation for incompressible flows: an introduction*. Springer Science & Business Media, 2006.
- [53] K. Samiei, B. Peters, M. Bolten, and A. Frommer. Assessment of the potentials of implicit integration method in discrete element modelling of granular matter. *Computers & Chemical Engineering*, 49:183–193, feb 2013.
- [54] Miquel Santasusana, Joaquín Irazábal, Eugenio Oñate, and Josep Maria Carbonell. The Double Hierarchy Method. A parallel 3D contact method for the interaction of spherical particles with rigid FE boundaries using the DEM. *Computational Particle Mechanics*, 3(3):407–428, jul 2016.
- [55] Subhash N. Shah, Youness El Fadili, and R. P. Chhabra. New model for single spherical particle settling velocity in power law (visco-inelastic) fluids. *International Journal of Multiphase Flow*, 33(1):51–66, 2007.
- [56] Shankar Subramaniam. Lagrangian–eulerian methods for multiphase flows. *Progress in Energy and Combustion Science*, 39(2-3):215–245, 2013.
- [57] C. Thornton. A note on the effect of initial particle spin on the rebound behaviour of oblique particle impacts. *Powder Technology*, 192(2):152–156, jun 2009.
- [58] Colin Thornton, Sharen J. Cummins, and Paul W. Cleary. An investigation of the comparative behaviour of alternative contact force models during inelastic collisions. *Powder Technology*, 233:30–46, jan 2013.
- [59] Gordon A Tibbitts and Greg G Galloway. Particle drilling alters standard rock-cutting approach: Drilling/completions. *World oil*, 229(6), 2008.
- [60] K. T. Trinh. On The Critical Reynolds Number For Transition From Laminar To Turbulent Flow. page 39, jul 2010.
- [61] L. Wakaba and S. Balachandar. On the added mass force at finite Reynolds and acceleration numbers. *Theoretical and Computational Fluid Dynamics*, 21(2):147–153, mar 2007.

- [62] Tamer M Wasfy and Ahmed K Noor. Computational strategies for flexible multi-body systems. *Appl. Mech. Rev.*, 56(6):553–613, 2003.
- [63] CM Wensrich and A Katterfeld. Rolling friction as a technique for modelling particle shape in dem. *Powder Technology*, 217:409–417, 2012.
- [64] J.R. Williams and R. O’Connor. A linear complexity intersection algorithm for discrete element simulation of arbitrary geometries. *Engineering Computations*, 12(2):185–201, feb 1995.
- [65] CM Winkler and Sarma L Rani. Relative importance of the lift force on heavy particles due to turbulence driven secondary flows. *Powder technology*, 190(3):310–318, 2009.
- [66] W. L. Wood, M. Bossak, and O. C. Zienkiewicz. An alpha modification of Newmark’s method. *International Journal for Numerical Methods in Engineering*, 15(10):1562–1566, oct 1980.
- [67] Tingjun Yan, Jinghao Li, and Linna Zhao. Numerical simulation on flow field of particle impact drilling in different drilling parameters. *DEStech Transactions on Computer Science and Engineering*, (Icte):1–5, 2016.
- [68] Weidong Zhou, Jinsong Huang, and Luopeng Li. Numerical simulation of bottomhole flow field structure in particle impact drilling. *E&ES*, 108(3):032080, 2018.